### **OPEN ACCESS**



# **Active Galactic Nucleus Quenching in Simulated Dwarf Galaxies**

Ray S. Sharma<sup>1</sup>, Alyson M. Brooks<sup>1,2</sup>, Michael Tremmel<sup>3</sup>, Jillian Bellovary<sup>4,5,6</sup>, and Thomas R. Quinn<sup>7</sup> Department of Physics and Astronomy, Rutgers, The State University of New Jersey, 136 Frelinghuysen Road, Piscataway, NJ 08854, USA Ramon.Sharma1@gmail.com

<sup>2</sup> Center for Computational Astrophysics, Flatiron Institute, 162 Fifth Avenue, New York, NY 10010, USA
 <sup>3</sup> Department of Astronomy, Yale University, 52 Hillhouse Avenue, New Haven, CT 06511, USA
 <sup>4</sup> Department of Physics, Queensborough Community College, City University of New York, 222–05 56th Avenue, Bayside, NY 11364, USA
 <sup>5</sup> Department of Astrophysics, American Museum of Natural History, Central Park West at 79th Street, New York, NY 10024, USA
 <sup>6</sup> The Graduate Center, City University of New York, 365 5th Avenue, New York, NY 10016, USA
 <sup>7</sup> Department of Astronomy, University of Washington, P.O. Box 351580, Seattle, WA 98195, USA
 Received 2022 November 9; revised 2023 June 14; accepted 2023 June 19; published 2023 October 20

#### **Abstract**

We examine the quenching characteristics of 328 isolated dwarf galaxies ( $10^8 < M_{\rm star}/M_{\odot} < 10^{10}$ ) within the ROMULUS25 cosmological hydrodynamic simulation. Using mock-observation methods, we identify isolated dwarf galaxies with quenched star formation and make direct comparisons to the quenched fraction in the NASA Sloan Atlas (NSA). Similar to other cosmological simulations, we find a population of quenched, isolated dwarf galaxies below  $M_{\rm star} < 10^9 M_{\odot}$  not detected within the NSA. We find that the presence of massive black holes (MBHs) in ROMULUS25 is largely responsible for the quenched, isolated dwarfs, while isolated dwarfs without an MBH are consistent with quiescent fractions observed in the field. Quenching occurs between z = 0.5-1, during which the available supply of star-forming gas is heated or evacuated by MBH feedback. Mergers interactions seem to play little to no role in triggering the MBH feedback. At low stellar masses,  $M_{\rm star} \lesssim 10^{9.3} M_{\odot}$ , quenching proceeds across several Gyr as the MBH slowly heats up gas in the central regions. At higher stellar masses,  $M_{\rm star} \gtrsim 10^{9.3} M_{\odot}$ , quenching occurs rapidly within 1 Gyr, with the MBH evacuating gas from the central few kpc of the galaxy and driving it to the outskirts of the halo. Our results indicate the possibility of substantial star formation suppression via MBH feedback within dwarf galaxies in the field. On the other hand, the apparent overquenching of dwarf galaxies due to MBH suggests that higher-resolution and/or better modeling is required for MBHs in dwarfs, and quenched fractions offer the opportunity to constrain current models.

*Unified Astronomy Thesaurus concepts:* Dwarf galaxies (416); Supermassive black holes (1663); Star formation (1569); Active galaxies (17); Galaxy quenching (2040); Hydrodynamical simulations (767)

# 1. Introduction

Over the past two decades, large sky surveys have found a bimodality in galaxy properties that separate actively star-forming galaxies from quiescent galaxies as far back as z=4 (Giallongo et al. 2005; Willmer et al. 2006; Cassata et al. 2008; Brammer et al. 2009; Ilbert et al. 2013; Muzzin et al. 2013). Galaxies occupy distinct regions in the color–magnitude (or similarly color–color, star formation rate–mass) space, where star-forming galaxies exhibit younger, bluer stellar populations in rotation-dominated morphologies, while quiescent galaxies exhibit older, redder populations in dispersion-dominated morphologies (Strateva et al. 2001; Bell et al. 2003; Kauffmann et al. 2003b; Baldry et al. 2004, 2006; Balogh et al. 2004; Wyder et al. 2007; Gallazzi et al. 2008; Ilbert et al. 2010; McGee et al. 2011; Wetzel et al. 2012; López Fernández et al. 2018)

Observations by Peng et al. (2010) have shown that galaxies may cease star formation through two distinct quenching pathways: through environmental quenching (Baldry et al. 2004; Kauffmann et al. 2004; Bahé & McCarthy 2015) via galaxy harassment (Feldmann et al. 2010), tidal stripping, or ram pressure stripping (Tonnesen et al. 2007; Weinmann et al. 2009); or through mass/internal quenching (Kauffmann et al. 2003a)

Original content from this work may be used under the terms of the Creative Commons Attribution 4.0 licence. Any further distribution of this work must maintain attribution to the author(s) and the title of the work, journal citation and DOI.

via, e.g., halo quenching in massive halos (Rees & Ostriker 1977; Kauffmann et al. 1993) or starvation (Larson 1974; Dekel & Silk 1986) in both low- and high-mass halos. Internal quenching mechanisms also include the physical removal or heating of star-forming gas via feedback from stars and active galactic nuclei (AGN; e.g., Choi et al. 2015, 2018). The standard paradigm explains that the low-mass end of the galaxy stellar mass function is suppressed by reionization (Efstathiou 1992; Okamoto et al. 2008; Fitts et al. 2017; Rey et al. 2019, 2020; Applebaum et al. 2021; Munshi et al. 2021) and supernovae (SNe) feedback (Larson 1974; Dekel & Silk 1986; Mori et al. 2002), while the high-mass end is regulated by AGN feedback (Binney & Tabor 1995; Di Matteo et al. 2005; Bower et al. 2006; Croton et al. 2006; Sijacki et al. 2007; Cattaneo et al. 2008).

Among low-mass galaxies in particular, it is well-known that high-density environments may quench star formation through environmental quenching processes (e.g., van den Bosch et al. 2008; Smith et al. 2012; Wetzel et al. 2013, 2014; Bahé & McCarthy 2015; Weisz et al. 2015; Tinker et al. 2017; Simpson et al. 2018; Akins et al. 2021; Samuel et al. 2022, though, see Emerick et al. 2016), and indeed quenched dwarf galaxies are thought to be exceedingly rare in the field (Geha et al. 2012). Only in recent years have internal processes been observed to quench dwarf galaxies in isolation (Janz et al. 2017). It is worth noting that among the lowest-mass dwarfs  $(M_{\rm vir} \lesssim 10^8 M_{\odot})$ , there is observational evidence that cosmic reionization may have quenched low-mass dwarfs around  $z \sim 6$ 

(e.g., Brown et al. 2014; Weisz et al. 2014; Bettinelli et al. 2018), though other work finds no such signal (Monelli et al. 2010; Hidalgo et al. 2011; Skillman et al. 2017).

Observational evidence is building that suggests AGN feedback may impact star formation in dwarf galaxies (Silk 2017). Using Mapping Nearby Galaxies at Apache Point Observatory (MaNGA) observations of quenched galaxies with stellar masses  $M_{\rm star} < 5 \times 10^9 M_{\odot}$ , Penny et al. (2018) identify six quenched galaxies that exhibit offsets between star and gas kinematics alongside strong AGN-like ionization, indicative of star formation suppression driven by AGN feedback. Bradford et al. (2018) use unresolved HI measurements to identify a population of  $10^{9.2} < M_{\rm star}/M_{\odot} < 10^{9.5}$  galaxies with quiescent star formation, gas depletion, and strong AGN-like ionization. Manzano-King et al. (2019) present the first direct detection of high-velocity, AGN-driven ionized gas outflows within a sample of 13 optically selected dwarf galaxies with  $10^{8.78} < M_{\rm star}/M_{\odot} < 10^{9.95}$ . Of these galaxies, six have AGNlike line ratios alongside outflow velocities exceeding the escape velocity of the host halo. Dickey et al. (2019) perform follow-up optical spectroscopy of the lowest-mass quiescent dwarfs known to exist in isolation, finding that 16 of the 20 observed quiescent dwarfs show signs of strong AGN-like line ratios. They find that the AGN fraction among isolated, quiescent galaxies is significantly higher than for quiescent dwarfs in group environments.

Some simulations and analytic models of low-mass galaxies have also begun to find that AGN feedback may have a greater impact on star formation than previously thought. By assuming standard massive black hole (MBH) scaling relations, Dashyan et al. (2018) use analytic models to show that feedback from AGN may be even more successful than SNe in driving out gas from galaxies below a critical halo mass threshold. Using a suite of cosmological simulations run with various MBH and SN feedback models, Barai & Pino (2019) find that gas-rich dwarf galaxies  $(10^5 < M_{\rm star}/M_{\odot} < 10^8$  at z = 4) can quench at z = 5 - 9 from early AGN feedback, and only the hosts of the most massive MBHs show signatures of AGN-driven outflows. Sharma et al. (2020) explore the impact of MBHs in isolated  $10^8 < M_{\rm star}/M_{\odot} < 10^{10}$  dwarfs in ROMULUS25, finding that efficiently accreting MBHs are more likely than inefficient accretors to be found within diffuse, gas-depleted, quiescent galaxies. Within the FABLE cosmological simulations, Koudmani et al. (2021) find that overmassive (relative to the BH mass– $M_{\rm star}$  relation) MBHs in  $M_{\rm star}$  <  $10^{9.5} M_{\odot}$  galaxies are able to drive hotter, faster outflows, which drive material out of the host halo. They find that outflows from overmassive MBHs are strong enough to suppress star formation at high redshift, driving misalignment of the stellar and ionized gas kinematics. At z < 2, their AGN exhibit lower accretion rates on average, and SNe feedback becomes the more dominant driver of star formation suppression. Using a suite of cosmological zoom simulations of a  $M_{\rm vir}(z=0) \sim 10^{10} M_{\odot}$  halo, Koudmani et al. (2022) find that feedback from overmassive MBHs may regulate star formation with effects ranging from minor suppression to catastrophic quenching. Their MBHs are capable of driving ejective outflows that deplete (or partially deplete) the star-forming gas reservoir. Quiescence is maintained through the AGN heating the circumgalactic medium and suppressing future cold gas accretion into the galaxy.

On the other hand, some simulations find that MBH feedback is subdominant to SNe feedback in impacting star

formation. Habouzit et al. (2017) find that SNe-driven winds within low-mass SUPERCHUNKY halos ( $M_{\rm halo} \lesssim 10^{11} M_{\odot}$ ) can remove dense, star-forming gas, and inhibit gas accretion onto the central MBHs. Koudmani et al. (2019) test various AGN and SN feedback models in high-resolution simulations of a  $M_{\rm star} \sim 2 \times 10^9 M_{\odot}$  dwarf galaxy. They find that AGN can drive hotter, higher velocity outflows, which are in line with the results from Penny et al. (2018), but alone are unable to drive global changes in star formation. In their simulations, it is the combination of AGN feedback and SN feedback that can impact star formation.

Cosmological simulations have only in recent years achieved the resolutions and complexity to be able to accurately study quenching in galaxies at Milky Way masses and below (e.g., Kimm et al. 2015; Joshi et al. 2021; Sanchez et al. 2021; Davies et al. 2022). In the past, simulations have struggled to generate consistent fractions of quenched satellite galaxies (Weinmann et al. 2006; Font et al. 2008; Kimm et al. 2009; Hirschmann et al. 2014; Somerville & Davé 2015). Now, simulations can better reproduce the observed bimodal distributions in the star formation rate (SFR; Feldmann et al. 2017), morphology (Snyder et al. 2015), and color (Nelson et al. 2018; Akins et al. 2021). However, Dickey et al. (2021) find that large-scale cosmological simulations tend to overpredict the numbers of isolated, quiescent galaxies between  $10^8 < M_{\rm star}/M_{\odot} < 10^{10}$ . Even when accounting for observational and selection biases as well as differences in resolution, cosmological simulations tend to quench dwarf galaxies more often than observed in the optical.

In this work, we analyze the characteristics of isolated, quiescent dwarf galaxies in the ROMULUS25 cosmological hydrodynamical simulation. We select our sample using the mock-observation process introduced in Dickey et al. (2021), allowing us to make direct comparisons with optical observations and other mock-observed simulations. In Section 2 we outline the relevant physics in the simulation, as well as the mock-observation procedure used in this work. In Section 3, we explore the differences in the star formation histories, stellar morphologies, gas contents, and gas evolutions between quiescent and star-forming dwarfs between  $10^8 < M_{\rm star}/M_{\odot} <$ 10<sup>10</sup>. We further investigate the quenching mechanism in our isolated dwarfs, assessing the impact of both environment and feedback effects on star formation suppression. ROMULUS25 is well-equipped for this analysis as one of few large-scale cosmological simulations capable of resolving the growth and dynamics of MBHs in low-mass galaxies, allowing us to accurately assess their importance to low-mass galaxy quenching.

#### 2. Methods

# 2.1. Simulation

Here we summarize the relevant aspects of the ROMULUS25 cosmological hydrodynamical simulation. The full description of the physical prescriptions can be found in Wadsley et al. (2017) and Tremmel et al. (2017).

The ROMULUS suite of cosmological hydrodynamic simulations was run with the Tree+SPH code CHANGA (Menon et al. 2015; Wadsley et al. 2017). In the ROMULUS25 (25 Mpc)<sup>3</sup> uniform-resolution volume, dark matter particles have masses of  $3.39 \times 10^5 M_{\odot}$  while gas particles have masses of  $2.12 \times 10^5 M_{\odot}$ . Particles have a Plummer equivalent force

softening of 250 pc. ROMULUS25 contains 3.375× more dark matter particles than gas in order to better resolve the dynamics of MBHs (Tremmel et al. 2015). ROMULUS25 uses a Planck 2014  $\Lambda$ CDM cosmology, with  $\Omega_m = 0.3086$ ,  $\Omega_{\Lambda} = 0.6914$ , h = 0.6777, and  $\sigma_8 = 0.8288$  (Planck Collaboration et al. 2014).

Star formation is governed by the star formation efficiency, SN feedback efficiency, and gas density threshold for star formation. Star formation follows a Kroupa (2001) initial mass function. These free parameters were tuned in Tremmel et al. (2017) with a suite of 80 zoom simulations of halos with halo masses  $M_{\rm vir} = 10^{10.5} - 10^{12} M_{\odot}$ . The star formation parameters were chosen by their ability to reproduce local scaling relationships between the stellar mass, halo mass, HI gas mass, and angular momentum (Cannon et al. 2011; Haynes et al. 2011; Moster et al. 2013; Obreschkow & Glazebrook 2014), resulting in the following star formation parameters:

- 1. Star formation efficiency,  $c_* = 0.15$ ,
- 2. SN feedback efficiency,  $\epsilon_{\rm SN} = 0.75$ , 3. Gas density threshold,  $n_* = 0.2~m_p~{\rm cm}^{-3}$ .

ROMULUS25 also contains models for metal diffusion (Shen et al. 2010), thermal diffusion (Governato et al. 2015), and lowtemperature radiative cooling (Guedes et al. 2011).

MBHs are seeded similar to a direct-collapse model (Haiman 2013; Greene et al. 2020), using properties of local, pre-collapse gas. Gas particles form MBH seeds if they follow these criteria:

- 1. Low metallicity,  $Z < 3 \times 10^{-4}$ ,
- 2. Gas density threshold,  $n_* > 3$   $m_p$  cm<sup>-3</sup>, 3. Temperature,  $T \sim 10^4$  K,

which were chosen to restrict BH seeding to form gas that is both collapsing rapidly and cooling slowly. These criteria approximate the seeding environments from theoretical estimates (Begelman et al. 2006; Volonteri 2012). Once the gas particle meets these criteria, it seeds an MBH with mass  $M_{\rm BH} = 10^6 M_{\odot}$ , gathering mass from nearby gas particles if necessary. These criteria restrict nearly all MBH seeding to above redshift  $z \gtrsim 5$ .

Dynamical friction prescriptions are employed in ROMU-LUS25 in order to realistically model MBH sinking timescales (Tremmel et al. 2015). Dynamical friction subgrid models allow MBHs in large halos to stay centered (Kazantzidis et al. 2005; Pfister et al. 2017) without forced MBH re-centering. This prescription also allows for "wandering" MBHs, which move more freely throughout shallow potentials, as has been discovered in recent work (Bellovary et al. 2019; Reines et al. 2020; Ricarte et al. 2021a, 2021b). The oversampling of dark matter, the high MBH seed mass, and the dynamical friction prescription together mitigate unrealistic numerical heating of MBHs, ensuring accurate MBH dynamics.

Feedback from MBHs follows a modified blast-wave SN feedback model (Stinson et al. 2006), where thermal energy is isotropically injected into the 32 nearest gas particles within some time, dt, following:

$$E_{\rm BH} = \epsilon_r \epsilon_f \dot{M} c^2 dt, \tag{1}$$

where  $E_{\rm BH}$  is the injected thermal energy,  $\epsilon_r = 0.1$  the radiative efficiency,  $\epsilon_f = 0.02$  the energy injection efficiency, and  $\dot{M}$  the MBH accretion rate. MBH accretion in ROMULUS25 follows a modified Bondi-Hoyle prescription that accounts for angular momentum on resolved spatial scales while enforcing Eddington-limited accretion. Accretion is handled on the smallest simulation time resolution element, typically  $10^4$ – $10^5$  yr.

The free parameters for MBH accretion and feedback were tuned through an additional 48 zoom simulations of the same halos used for star formation parameter tuning. Instead, the star formation parameters were fixed while the MBH parameters were allowed to vary in order to match the observed z = 0 BH mass-stellar mass relation (Schramm & Silverman 2013).

In this work, we use the Amiga Halo Finder (Knollmann & Knebe 2009) to extract gravitationally bound dark matter halos, subhalos, and their corresponding baryonic content. AHF defines the virial radius,  $R_{\text{vir}}$ , and virial mass,  $M_{\text{vir}}$ , using a spherical top-hat collapse technique. Each halo center is estimated using a shrinking spheres approach (Power et al. 2003). When discussing halo masses, we define

$$M_{200} = 4\pi \rho_c \times 200 R_{200}^3, \tag{2}$$

where  $\rho_{\rm c}$  is the cosmic critical density, and  $R_{200}$  is the halo

#### 2.2. Mock Observations

In order to make direct comparisons of simulation results with observations, we use the mock-observation package orchard<sup>8</sup> (Dickey et al. 2021). The orchard package was designed to allow direct comparisons of galaxy-quenched fractions between uniform cosmological simulations and observations. By adding realistic noise and observational limits to synthetic spectra, orchard accounts for the effects of observational incompleteness, finite signal-to-noise ratio (S/N), and imprecise distance information for galaxies in a wide-field survey. In the following sections, we outline the mock-observation procedure.

# 2.2.1. Synthetic Spectra

Following Dickey et al. (2021), we first generate synthetic spectra for each target galaxy using stellar population synthesis models from FLEXIBLE STELLAR POPULATION SYNTHESIS (FSPS; Conroy et al. 2009; Conroy & Gunn 2010) with the Python interface python-fsps (Dan Foreman-Mackey & Johnson 2014). When generating spectra, we use a Chabrier (2003) initial mass function (IMF) to match the assumed IMF from Dickey et al. (2021). For each galaxy at z = 0.05, we bin the total stellar mass across a uniform grid of formation age and stellar metallicity. Formation age bins increase linearly with look-back time,  $\tau$ , between  $\tau = [0, 13.1]$  Gyr. Metallicity bins run between  $\log_{10}(Z/Z_{\odot}) = [-2.2, 0.5]$  with bin size  $\Delta Z = 0.3$ at low metallicity, increasing to  $\Delta Z = 0.1$  near Z = 0. To avoid resolution effects on the most recent star formation, we calculate SFRs younger than 15 Myr using the expected instantaneous SFR from the gas particles that meet the temperature and density criteria necessary to form stars.

Nebular emission lines are calculated by FSPS within each metallicity bin using a CLOUDY lookup table (Byler et al. 2017) with gas metallicity set to the bin metallicity. We also include the effects of dust on our synthetic spectra. We use the Villaume et al. (2015) dust emission model for asymptotic giant branch stars. We use the two-component dust model from

<sup>8</sup> https://github.com/IQcollaboratory/orchard

 $10^{10}$ 

Charlot & Fall (2000), with a power-law dust attenuation index  $\Gamma = 0.7$  and normalization  $\tau(5500\,\text{Å}) = 0.33$ . Stars younger than 30 Myr have additional attenuation, with an index  $\Gamma = 0.7$  and normalization  $\tau(5500\,\text{Å}) = 1.0$ . To produce a galaxy spectrum, we sum the spectra of all stellar populations in each bin of the t, Z grid, weighting by the stellar mass formed.

#### 2.2.2. Mock Survey

We next generate a mock survey emulating Sloan Digital Sky Survey (SDSS) observing characteristics using basic halo properties along with the synthetic spectra. The detailed steps are outlined in Dickey et al. (2021), which we summarize as follows:

- 1. Select a random location 10 Mpc outside the simulation volume to place a mock observer.
- 2. Calculate apparent SDSS *g* and *r*-band magnitudes, radial velocity, and projected distance for all galaxies as the observer would see them on the sky.
- 3. Convolve each noise-free, synthetic spectrum with the SDSS instrumental line-spread profile and resample to match the SDSS wavelength resolution and coverage. We model the line-spread profile as a Gaussian with  $\sigma = 70 \text{ km s}^{-1}$ .
- 4. Add SDSS-like noise to each spectrum in the mock observer's frame, using the average S/N at each wavelength found by Dickey et al. (2021). Noise is added based on the galaxy color, apparent magnitude, and wavelength by drawing from a normal distribution  $\sigma(\lambda, g r, m_r)$ .
- 5. Measure  $D_{\rm n}4000$  (Balogh et al. 1999) and the H $\alpha$  equivalent width (EW; Yan et al. 2006) from the noise-added, instrumentally broadened spectra.

From these noise-added measurements of  $D_{\rm n}4000$  and  $H\alpha$  EW, we are able to identify quiescent galaxies within ROMULUS25 as an observer might, along a given line of sight. The  $H\alpha$  EW traces star formation within the past 10 Myr, while  $D_{\rm n}4000$  probes long-term star formation over the past 1 Gyr by quantifying the strength of the 4000 Å break in each noise-added spectrum (Balogh et al. 1999; Brinchmann et al. 2004). We consider a galaxy along a given sight line to be quiescent if  $H\alpha$  EW < 2 Å and  $D_{\rm n}4000 > 0.6 + 0.1 \log_{10} M_{\rm star}$  (Geha et al. 2012).

Figure 1 shows the relationship between the intrinsic SFR and  $M_{\rm star}$  among the isolated dwarf galaxies in ROMULUS25 at z=0.05 (see Section 3 for further explanation). In the top panel, we calculate the instantaneous SFR using the expected SFR from gas particles meeting the temperature and density thresholds for star formation. In the bottom panel, we average the SFR over the past 100 Myr. We distinguish between galaxies identified by orchard as quiescent (red circles) versus star-forming (blue circles), where quiescence is determined indirectly from the noise-added H $\alpha$  EW and  $D_{\rm n}4000$  for a single sight line. As in Dickey et al. (2021), we only show galaxies brighter than an r-band apparent magnitude of  $m_r < 17.7$  and r-band surface brightness of  $\mu_r < 23$  mag arcsec<sup>-2</sup>.

Following Ricarte et al. (2019), we calculate the star formation main sequence in ROMULUS25 by fitting the median SFR of star-forming galaxies in 0.1 dex stellar mass bins between  $10^8 < M_{\rm star}/M_{\odot} < 10^{10}$ , estimating the uncertainty with interquartile ranges. We calculate both the instantaneous

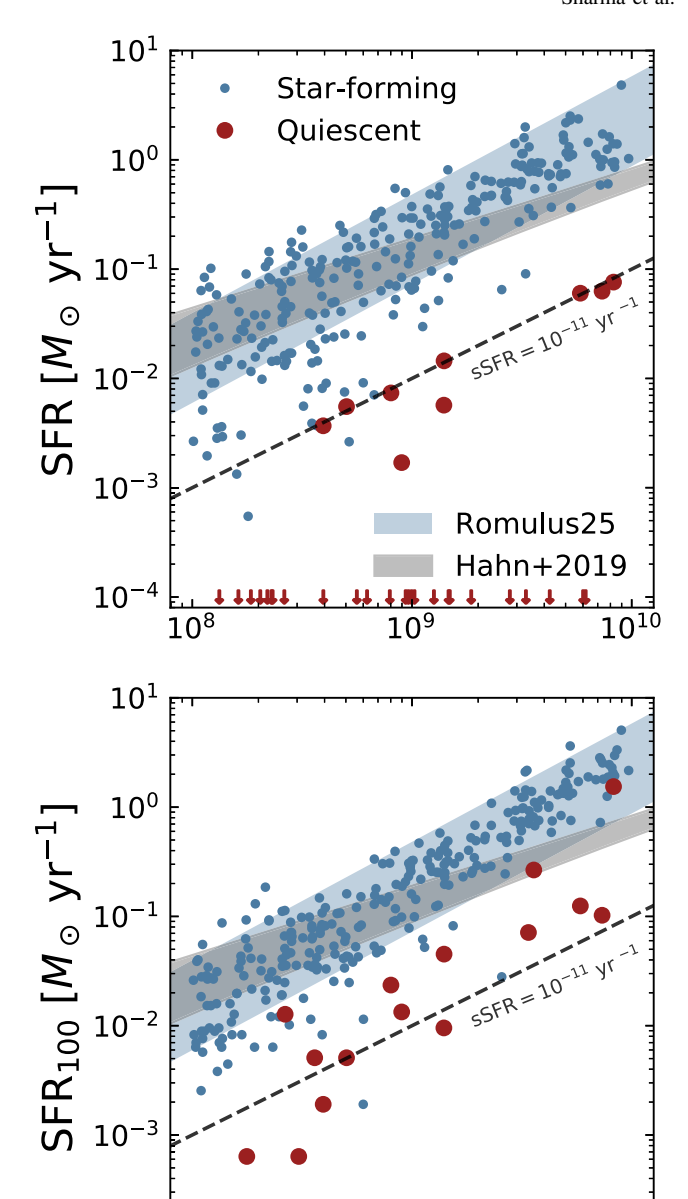


**Figure 1.** Instantaneous (top) and 100 Myr averaged (bottom) intrinsic SFR vs. stellar mass for isolated dwarfs at z=0.05. Quiescent dwarfs (red circles) selected through H $\alpha$  EW and  $D_{\rm n}4000$  exhibit lower SFRs at fixed stellar mass than star-forming dwarfs (blue dots). The SFR- $M_{\rm star}$  relation derived from star-forming dwarfs (blue-shaded interquartile range) approximately agrees with the main sequence found from SDSS (Hahn et al. 2019), though simulation SFRs are slightly overpredicted at the highest masses shown. 64% of isolated, quiescent dwarfs in ROMULUS25 have 100 Myr averaged SFR below  $10^{-4}M_{\odot}~{\rm yr}^{-1}$ .

 $M_{\rm star} [M_{\odot}]$ 

SFR and 100 Myr averaged SFR from the simulation to better compare with the SDSS-derived SFRs found in Hahn et al. (2019). They combine the SDSS Data Release 7 massive, central galaxy sample from Tinker et al. (2011) with the NASA Sloan Atlas low-mass, isolated galaxy sample from Geha et al. (2012). Their sample spans stellar masses  $10^8 M_{\odot} \lesssim M_{\rm star} \lesssim 10^{12} M_{\odot}$  at  $z \sim 0$  (see Hahn et al. 2019 for more details). The observations exhibit a slope of SFR  $\propto M_{\rm star}^{0.69}$ .

Isolated dwarf galaxies in ROMULUS25 exhibit a similar main sequence to the observations down to  $M_{\rm star}=10^8 M_{\odot}$ , albeit with a steeper slope, SFR  $\propto M_{\rm star}^{1.08}$ , for our sample.

Because our quiescent definition probes the luminosityweighted stellar age rather than the SFR directly, there are cases of quiescent galaxies with higher average SFRs than starforming galaxies at a given stellar mass. Regardless, we find that galaxies indirectly identified as quiescent typically fall below the main sequence, with 63% of quiescent dwarfs exhibiting SFR  $< 10^{-4} M_{\odot} \text{ yr}^{-1}$  no matter how SFR is derived. Indirect identification of quiescent galaxies also tends to identify dwarfs below the commonly used specific star formation rate (sSFR) indicator of quiescence  $sSFR = 10^{-11} \text{ yr}^{-1}$  (black dashed; e.g., Wetzel et al. 2014). This tendency is particularly true when using instantaneous sSFRs, where 93% of quiescent dwarfs fall below the instantaneous sSFR threshold, versus the 73% of quiescent dwarfs that fall below the 100 Myr threshold. Overall, the ROMULUS25 quiescent fractions shown in Section 3.1 change little when defining quiescence through either cuts on sSFR, cuts on distance from the main sequence, or through *orchard*.

#### 3. Results

In order to analyze the quenching properties of simulated galaxies and compare them to observations, we must first make a correction to the simulated stellar masses. By comparing the stellar-to-halo mass relation from high-resolution hydrodynamical simulations to abundance-matching estimates, Munshi et al. (2013) find that stellar masses derived from aperture photometry tend to systematically underestimate the "true" stellar mass from simulations by around 50%. Similarly, Dickey et al. (2021) find that stellar masses derived from g-rcolors (Mao et al. 2021) and Bell et al. (2003) mass-to-light ratios tend to underestimate the "true" stellar mass by  $\sim 0.3$ dex. Previous studies of ROMULUS25 (e.g., Ricarte et al. 2019; Sharma et al. 2020) have typically used stellar mass corrections from Munshi et al. (2013). In order to stay consistent with the results from Dickey et al. (2021), we calculate stellar masses throughout this work using our measured g- and r-band magnitudes according to Mao et al. (2021):

$$\log (M_{\text{star}}/M_{\odot}) = 1.254 + 1.098(g - r) - 0.4M_r, \tag{3}$$

where  $M_r$  is the absolute r-band magnitude, assuming an absolute solar r-band AB magnitude of 4.64 (Conroy et al. 2009; Conroy & Gunn 2010). We confirm that the stellar masses derived using this approach are consistent (within 0.2 dex) with the adjusted stellar masses from previous works using ROMULUS25. Previous works incorporated a flat 60% correction to the raw simulated stellar masses, as motivated by results from Munshi et al. (2013). Regardless, we find that the choice of stellar mass correction has no impact on the measured quiescent fractions.

In this work we are primarily interested in dwarf galaxies between stellar masses  $10^8 < M_{\rm star}/M_{\odot} < 10^{10}$  at z=0.05. This mass range is just below the regime where feedback is often thought to change from SNe-dominated to AGN-dominated (e.g., Habouzit et al. 2017), as well as the regime where the MBH occupation fraction reaches unity in ROMU-LUS25 (Sharma et al. 2022).

In addition to selecting galaxies with low masses, we also set criteria on the galaxy local environment. We select isolated

Table 1
Summary of the Isolated Dwarf Galaxy Sample along the Sight Line used
Throughout this Work

	Star-forming	Quiescent	Total	
Central MBH	117	34	151	
Off-center MBH	17	1	18	
No MBH	152	7	159	
Total	286	42	328	

**Note.** We distinguish between star-forming versus quiescent galaxies, as well as galaxies with central MBHs (<2 kpc), off-center MBHs (>2 kpc), and galaxies entirely without MBHs.

galaxies following Geha et al. (2012) using cuts in the radial velocity and projected separation along the same single sight line. For each target galaxy, we first identify potential massive neighbors with  $M_{\rm star} > 2.5 \times 10^{10} M_{\odot}$  within an upper bound of 7 Mpc projected distance and relative radial velocity  $v_{\rm r} < 1000~{\rm km~s^{-1}}$ . We consider galaxies that have no massive neighbors within 1.5 projected Mpc ( $d_{\rm host} < 1.5~{\rm Mpc}$ ) to be isolated. Observations have found that galaxies with  $M_{\rm star} \lesssim 10^9 M_{\odot}$  are nearly all star-forming at this distance from a massive galaxy (Geha et al. 2012; Rasmussen et al. 2012; Penny et al. 2016). By following the isolation criteria, we mitigate the possibility of quenching from environmental effects (however, see Section 3.4 for an analysis of the possibility of splash-back galaxies).

There are instances in our analysis where we distinguish between dwarf galaxies with and without central MBHs. We define central MBHs as those within 2 kpc of the halo center. In cases where there are multiple MBHs (see, e.g., Tremmel et al. 2018), we define the central MBH to be the most massive within the central 2 kpc. Only a handful of galaxies in our sample host their most massive MBHs at large distances (>2 kpc) from the center.

Overall, these restrictions yield a sample of 328 well-resolved, isolated dwarf galaxies. Table 1 provides a breakdown of the sample along the single sight line used throughout much of this work.

#### 3.1. Dwarfs with MBHs are More Quiescent

We begin by examining the fraction of quiescent, isolated dwarf galaxies in ROMULUS25 following the methods from Dickey et al. (2021). We repeat our mock-observation process for 25 randomly selected sight lines outside the simulation box, remeasuring the noise-added  $D_{\rm n}4000$  and  $H\alpha$  EW values for each galaxy and ultimately identifying detectable quiescent galaxies for each sight line. In calculating the quiescent fraction, we weigh each galaxy by the inverse of the survey volume over which the galaxy could be observed given the SDSS spectroscopic magnitude limit,  $1/V_{\rm max}$ . We can hence write the quiescent fraction:

$$f_{\rm q} = \frac{\sum_{i=1}^{N_{\rm q}} 1/V_{{\rm max},i}}{\sum_{i=1}^{N_{\rm ull}} 1/V_{{\rm max},i}},\tag{4}$$

where  $N_{\rm q}$  and  $N_{\rm all} = N_{\rm q} + N_{\rm sf}$  are the numbers of quiescent and quiescent + star-forming galaxies in each mass bin, respectively. As in Dickey et al. (2021), we calculate the quiescent fraction for galaxies brighter than a limiting apparent

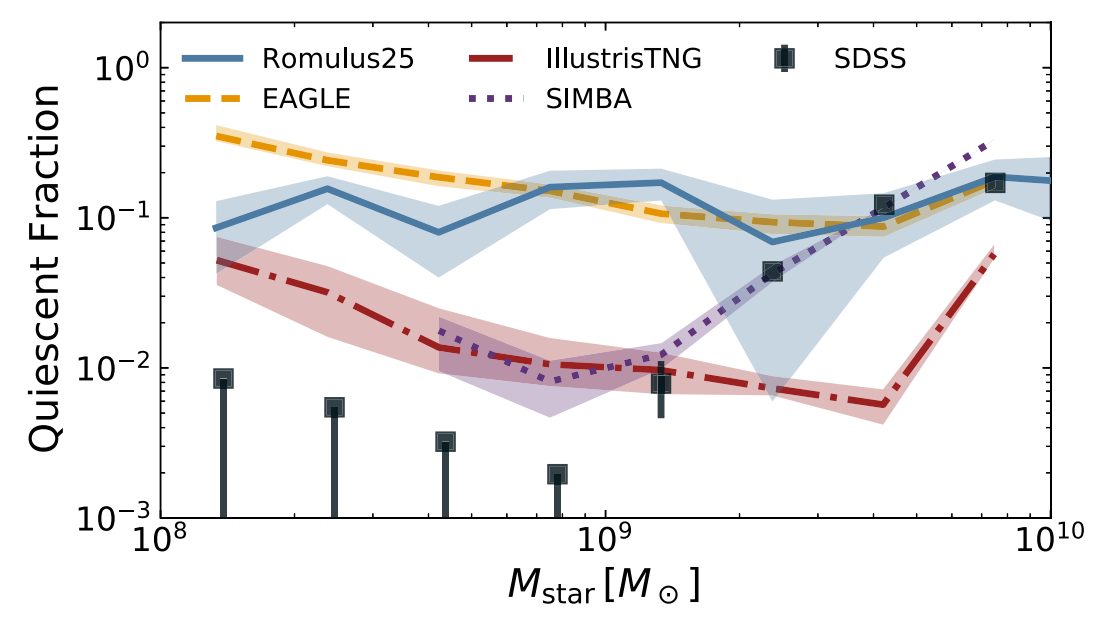


Figure 2. Quiescent fraction for isolated dwarf galaxies in ROMULUS25 (blue solid), EAGLE (yellow dashed), ILLUSTRISTNG (red dotted–dashed), SIMBA (purple dotted), and SDSS (Geha et al. 2012, black squares). Each curve represents the median across 25 randomly selected sight lines for galaxies above a limiting apparent magnitude of  $m_r = 17.7$  and an r-band surface brightness of  $\mu_r = 23$  mag arcsec<sup>-2</sup>, with the shaded regions representing the 95% binomial uncertainties averaged across all sight lines (see text for details). All simulations except ILLUSTRISTNG tend to reproduce the quiescent fraction for higher-mass dwarfs  $M_{\rm star} > 2 \times 10^9 M_{\odot}$ , but every simulation predicts  $5-15\times$  more quiescent low-mass dwarfs than found in observations.

magnitude of  $m_r = 17.7$ , and brighter than an r-band surface brightness of  $\mu_r = 23$  mag arcsec<sup>-2</sup>. Galaxies fainter than either limit along a given sight line are removed from the quiescent fraction calculation.

Figure 2 illustrates the z=0.05 quiescent fraction in ROMULUS25 as a function of the stellar mass. We show the median across all 25 sight lines, with uncertainties reflecting the 95% binomial uncertainties averaged across all N sight lines:

$$\sigma_{\text{tot}}^2 = \sum_{i} \frac{\sigma_i^2}{N}.$$

For comparison, we include the local quiescent fractions from the EAGLE (Schaye et al. 2015), ILLUSTRISTNG (Marinacci et al. 2018; Naiman et al. 2018; Nelson et al. 2018; Pillepich et al. 2018; Springel et al. 2018), and SIMBA (Davé et al. 2019) simulations, as calculated by Dickey et al. (2021) using *orchard* with the same mock-observation procedure, quiescent definition, and stellar mass definition. We also include the observed quiescent fraction from Geha et al. (2012) and Dickey et al. (2021) for mass-selected dwarf galaxies within z < 0.055 from the NASA/Sloan Atlas (Blanton et al. 2011).

Quiescent fractions in ROMULUS25 agree with observations down to  $M_{\rm star} > 2 \times 10^9 M_{\odot}$ , but overpredict the number of quiescent galaxies by  $10{\text -}100{\times}$  when moving to lower masses. As discussed in Dickey et al. (2021), all simulations (including ROMULUS25) find nonzero quiescent fractions for isolated dwarfs below  $M_{\rm star} < 10^9 M_{\odot}$ , in direct tension with SDSS observations. At  $M_{\rm star} = 10^9 M_{\odot}$ , ILLUSTRISTNG and SIMBA are closest with quiescent fractions  $\sim \! 1\%$ , while ROMULUS25 and EAGLE find quiescent fractions  $\sim \! 16\%$ . The weak dependence of quiescent fraction on stellar mass in ROMULUS25 is also most similar to EAGLE.

It is important to note that SDSS is likely incomplete at masses below  $M_{\rm star} < 10^9 M_{\odot}$ . Constraints on  $1/V_{\rm max}$ , and hence constraints on the quiescent fraction, are uncertain for

low luminosity and low-surface-brightness galaxies. Indeed, Thanjavur et al. (2016) find that the volume-corrected stellar mass function in SDSS-DR7 decreases below  $M_{\rm star} < 10^9 M_{\odot}$ , suggesting that the abundance of low-mass systems in SDSS is strongly underestimated. These results suggest that the quiescent fraction in dwarf galaxies would instead be higher than what is reported in Dickey et al. (2021), alleviating the discrepancy between observations and simulations.

Using deep optical imaging from the Hyper Suprime-Cam Subaru Strategic Program, Prole et al. (2020) identify a sample of 479 local (z < 0.2) low-surface-brightness galaxies (LSBs). Using estimates of the environmental densities to identify isolated LSBs, they measure a quiescent fraction for isolated LSBs of  $f_{\rm q} = 0.26 \pm 0.05$ . These quiescent fractions are consistent with ROMULUS25 quiescent fractions, yet substantially higher than observational constraints from Dickey et al. (2021). Prole et al. (2020) point out that several key studies (Martínez-Delgado et al. 2016; Román et al. 2019) have identified isolated quiescent galaxies, and hence the fraction of quiescent galaxies in the field is unlikely to be so close to zero.

We now illustrate the effects of central MBHs on the quiescence of dwarf galaxies. As before, we run *orchard* across 25 randomly chosen sight lines, but now separate isolated dwarfs hosting a central MBH from those entirely without an MBH. We define central MBHs as the most massive within 2 kpc of the halo center. Figure 3 shows the quiescent fraction for isolated dwarfs with central MBHs, and for those without MBHs. For comparison, we also include the observational constraints from Dickey et al. (2021).

Isolated dwarfs with central MBHs exhibit higher quiescent fractions than dwarfs without MBHs. Among dwarfs without any MBHs, the quiescent fraction is consistent with what is observed, varying between 0% and 8%. Among dwarfs with central MBHs, the quiescent fraction is substantially greater, varying between 15% and 30%. The overall quiescent fraction is largely driven by the quiescent fraction among dwarfs with

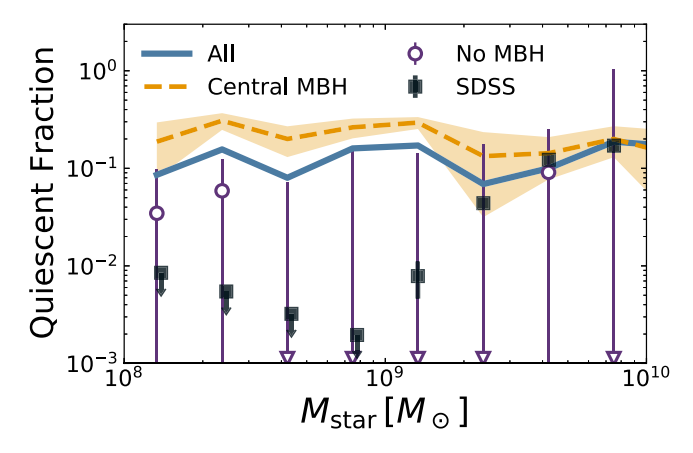


**Figure 3.** Median quiescent fraction across all 25 randomly selected sight lines (blue solid), highlighting the contribution from dwarfs with central MBH (yellow dashed) vs. dwarf galaxies entirely without MBHs (purple open circle). The median quiescent fraction for dwarfs without MBHs frequently falls below the lower limits of the figure, in which case they are marked by an unfilled arrow with upper limits on the uncertainties. Dwarfs with central MBHs are  $2-10\times$  more likely to be quiescent relative to dwarfs without MBHs. Dwarfs with central MBHs elevate the overall quiescent fraction for isolated dwarfs while dwarfs without MBHs exhibit quiescent fractions consistent with those found in SDSS at  $M_{\rm star} < 10^9~M_{\odot}$  (Geha et al. 2012, black squares).

MBHs. As shown in Sharma et al. (2022), the MBH occupation in ROMULUS25 begins to drop below  $M_{\rm star} \lesssim 10^{10} M_{\odot}$ . Despite being more rare in dwarf galaxies, the presence of MBHs appears to correlate with quiescence down to at least  $M_{\rm star} \sim 10^8 M_{\odot}$ .

It is worth noting that the MBH seeding mechanism and occupation fractions differ between each cosmological simulation we compare with. ILLUSTRISTNG forms an MBH within a halo once it reaches a mass threshold  $M_{\rm halo} > 5 \times 10^{10} M_{\odot}$  (Weinberger et al. 2017). EAGLE similarly seeds MBHs in halos that reach a halo mass  $M_{\rm halo} > 1.5 \times 10^{10} M_{\odot}$ . SIMBA instead seeds MBHs in galaxies with  $M_{\rm star} \gtrsim 10^{9.5} M_{\odot}$  (Davé et al. 2019). These cosmological simulations rarely (if ever) produce MBHs in halos at the lowest masses explored in this work. Thus, while our high quenched fractions at  $M_{\rm star} < 10^9 M_{\odot}$  appear to be connected to the presence of MBHs, MBHs are unlikely to be related to the high quenched fractions in dwarfs for other simulations.

We may also ask how detectable the MBHs in our dwarf galaxies are. Results from Sharma et al. (2022) indicate that ROMULUS25 dwarfs often host "hidden" MBHS that are undetectable to current instrumentation. Such MBHs exhibit one or more of the following traits: low X-ray luminosities in the 2–10 keV band ( $L_{\rm X}^{\rm AGN} < 10^{39} \, {\rm erg \ s^{-1}}$ ), low luminosities relative to X-ray contaminants ( $L_{\rm X}^{\rm AGN} < 2 \times L_{\rm X}^{\rm cont}$ ), and/or large distances from the halo center ( $d_{\rm BH} > 2 \, {\rm kpc}$ ).

Applying the same methodology from Sharma et al. (2022) to the dwarfs in our sample, we find that quiescent dwarfs are more likely to host hidden MBHs than star-forming dwarfs, but the majority of MBHs are not hidden. Among quiescent dwarfs with MBHs in our sample, 31% are hidden according to the criteria above, compared to the 21% of star-forming dwarfs. In other words, the majority of MBHs found in our dwarf sample are detectable to current X-ray instrumentation.

#### 3.2. Past Growth in Quiescent Dwarfs

With the knowledge that the presence of MBHs correlates with quiescence, we next examine the host galaxy properties in ROMULUS25. In order to understand how dwarf galaxies stop forming stars, it is important to understand the gas content of these dwarf galaxies and how they evolve over cosmic time. We explore the growth histories of our dwarfs via their cumulative star formation and H I gas mass histories. We also calculate the H I and total gas fractions for star-forming and quiescent dwarfs.

The left side of Figure 4 shows the individual cumulative star formation histories across cosmic time for quiescent galaxies along with the median for star-forming galaxies. Starting from z=0.05, we trace back the formation times and masses of all star particles. We divide our galaxies into bins of stellar mass at z=0.05. The shaded regions mark the interquartile ranges for star-forming galaxies. In each mass bin, we mark the median value of  $t_{90}$ , the cosmic time at which galaxies accumulate 90% of their maximum stellar mass.

As expected, quiescent dwarfs of all masses tend to follow different stellar growth tracks from star-forming dwarfs. Quiescent dwarfs tend to build up their stars at early times and then stop forming new stars, with median  $t_{90}$  approximately 5–8 Gyr ago, or redshift  $z \sim 0.5-1$ . Star-forming galaxies instead undergo steady formation of stars until the present day, building up their stellar component more slowly relative to quiescent galaxies. It is worth noting that not all quiescent dwarfs follow the schema of early stellar buildup and then quenching—a handful build up stars more slowly and stop at late times, following a stellar evolution closer to that of star-forming galaxies.

The right side of Figure 4 instead illustrates the history of  $M_{\rm HI}$  across the cosmic time for star-forming and quiescent galaxies, in the same stellar mass bins. Starting from z=0.05, we trace back the merger tree of each target halo and identify the main progenitor within each simulation snapshot, calculating the H I gas mass along the way. We show the median and interquartile ranges for star-forming galaxies and plot individual evolutionary tracks for the quiescent galaxies. We also mark the median values of  $t_{90}$  in each stellar mass bin for both quiescent and star-forming galaxies.

On average, quiescent galaxies tend to lose H I gas mass around the time of  $t_{90}$  and maintain low  $M_{\rm HI}$  afterward. Notably, 6 of the 42 isolated dwarfs that are quiescent at z=0.05 underwent a single replenishment of their H I gas supply, temporarily rejuvenating low levels of star formation in the recent past.

Similarly, we measure the sSFR across time for each isolated dwarf. To better distinguish the relative differences in sSFR tracks, we scale each track by  $\langle \text{sSFR}_{\text{sf}} \rangle$ , the mean sSFR for star-forming dwarfs within the same z=0.05 mass bin. The median tracks for each population are shown in Figure 5. We find that the cessation of star formation in quiescent dwarfs occurs around  $t_{90}$ , near the time that H I gas was found to deplete in Figure 4.

For each isolated dwarf, we next measure the neutral hydrogen gas fraction,  $M_{\rm HI}/M_{\rm star}$ , where  $M_{\rm HI}$  is the mass of gas held in an H I component; as well as the total gas fraction,  $M_{\rm gas}/M_{\rm star}$ , where  $M_{\rm gas}$  is the mass of all gas within the halo. Neutral hydrogen is primarily located within cool gas  $(T < 2 \times 10^4 \, {\rm K})$  and is a good tracer for the supply of star-forming gas within a galaxy.

The left panel of Figure 6 shows the H I gas fraction for isolated dwarf galaxies. We distinguish between star-forming and quiescent galaxies and compare with observed H I gas

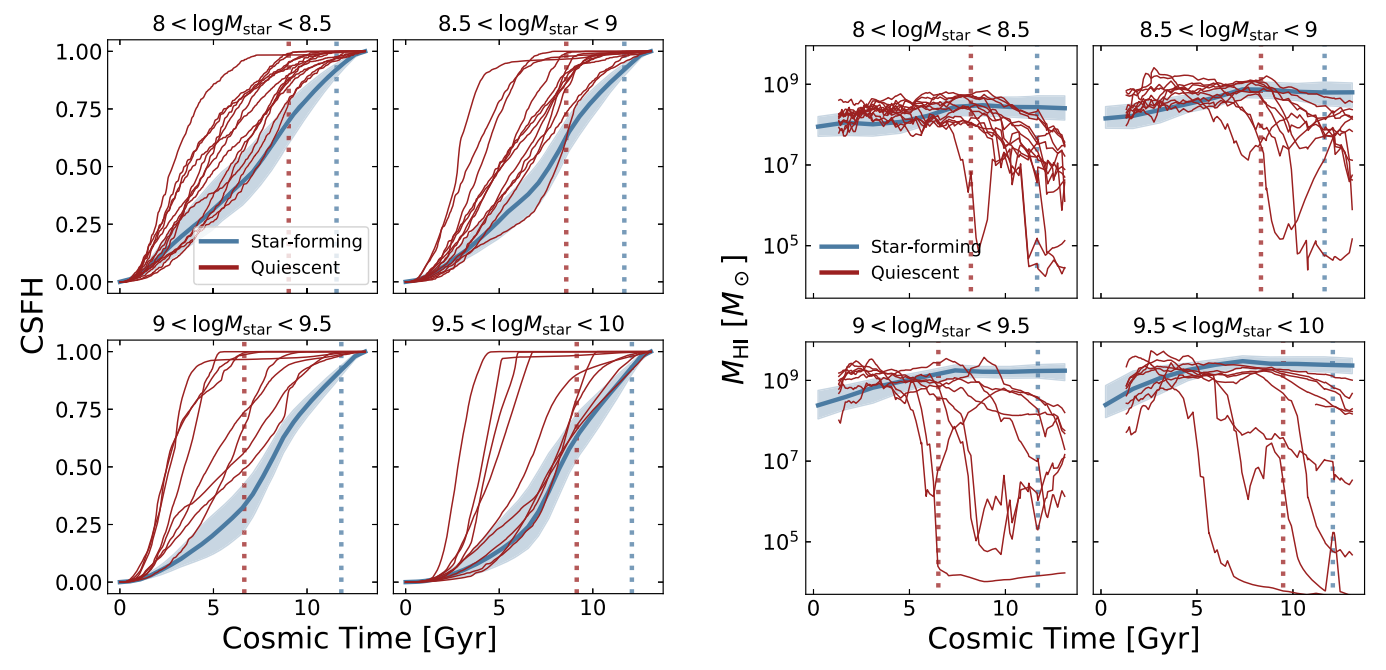


Figure 4. Cumulative star formation and H I gas mass growth for isolated dwarfs, binned by z = 0.05 stellar mass. Individual growth tracks are shown for quiescent dwarfs (red lines), while the median growth track for star-forming dwarfs (blue line) is shown with interquartile ranges. We show the median value of  $t_{90}$  for quiescent (red dashed) and star-forming (blue dashed) dwarfs. Left: cumulative star formation history over cosmic time for isolated dwarfs. In all panels, quiescent dwarfs grow stars more rapidly than star-forming dwarfs, and quench earlier. More massive dwarfs tend to quench at earlier times than less massive dwarfs, but all generally quench by redshift z = 0.5. Right: total mass of cool, star-forming H I gas as a function of the cosmic time. On average, star-forming dwarfs grow slowly in H I mass over time. The majority of quiescent dwarfs instead rapidly lose H I gas around the time of  $t_{90}$ , and remain devoid of H I. Six quiescent dwarfs regain small amounts of H I after the initial episode, reigniting low levels of star formation.

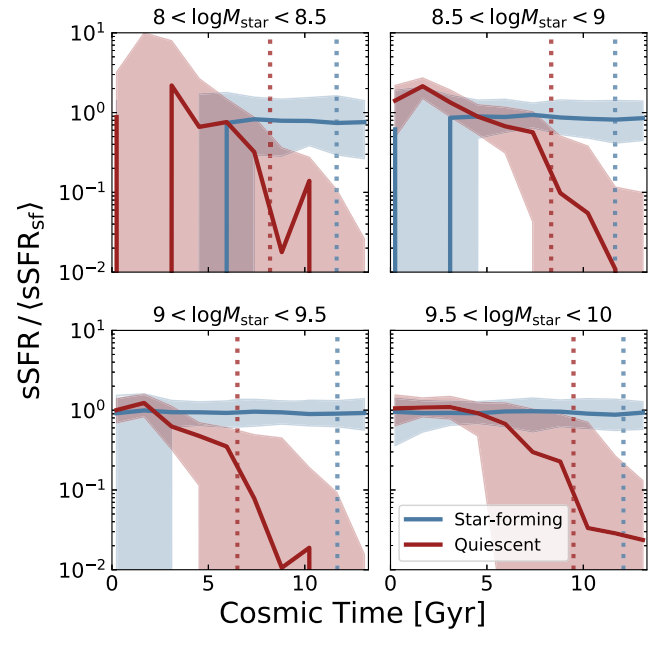


Figure 5. Similar to Figure 4, median growth tracks for specific star formation rate (sSFR) scaled by the mean sSFR for star-forming dwarfs in the same mass range. For clarity, we show only the median growth tracks for both quiescent dwarfs (red lines) and star-forming dwarfs (blue lines), along with their interquartile ranges. We show the median value of  $t_{90}$  for quiescent (red dashed) and star-forming (blue dashed) dwarfs. Quiescent dwarfs start with comparable levels of specific star formation at early times, then decrease in sSFR relative to star-forming dwarfs around  $t_{90}$ . By z = 0.05, quiescent dwarfs exhibit  $\lesssim 1$  dex lower sSFR.

fractions from the extended GALEX Arecibo SDSS survey (Catinella et al. 2018) and from combined Arecibo Legacy Fast ALFA (ALFALFA) 70% observations (Giovanelli et al. 2005;

Haynes et al. 2011) with follow-up Arecibo observations (Bradford et al. 2018). The sample from Catinella et al. (2018) is gas-fraction limited, with galaxies selected by stellar masses between  $10^9 < M_{\rm star}/M_{\odot} < 10^{11.5}$  out to z < 0.05. The sample from Bradford et al. (2018) includes unresolved H I observations from ALFALFA 70% along with deeper Arecibo observations of galaxies with stellar masses  $10^7 < M_{\rm star}/M_{\odot} < 10^{11.5}$  out to z < 0.055. The right panel of Figure 6 shows the total gas fraction for the same subsamples of dwarfs.

Quiescent dwarfs at all stellar masses exhibit a high degree of total gas depletion as well as  $\sim 1$  dex lower abundance of cool, star-forming gas. Star-forming dwarfs instead follow the observed relations between the HI gas fraction and  $M_{\rm star}$ . Depletion of H I gas is indicative of interstellar medium (ISM) heating and dispersal, while depletion of total gas indicates the ISM and circumgalactic medium are being removed from the halo entirely. The depleted H I gas fractions among quiescent dwarfs are consistent with observations, which find that low sSFRs correlate with HI gas depletion among a sample of 25,000 mass-selected, low-redshift galaxies from SDSS with HI detections from ALFALFA (Brown et al. 2015). Quiescent galaxies exhibit diminished total gas fraction, though to a lesser degree than is found among HI gas fractions. In other words, nearly all quiescent dwarfs show evidence of ISM heating, but not all quiescent dwarfs have had significant amounts of gas removed entirely from the halo. It is worth noting that the agreement of star-forming galaxies with observed relations follows from the simulation parameter tuning process (Tremmel et al. 2017), where the specific parameters controlling star formation were tuned to match HI gas fractions from SHIELD + ALFALFA (Cannon et al. 2011; Haynes et al. 2011). However, the relationship of quiescence with gas depletion is a prediction of the simulation.

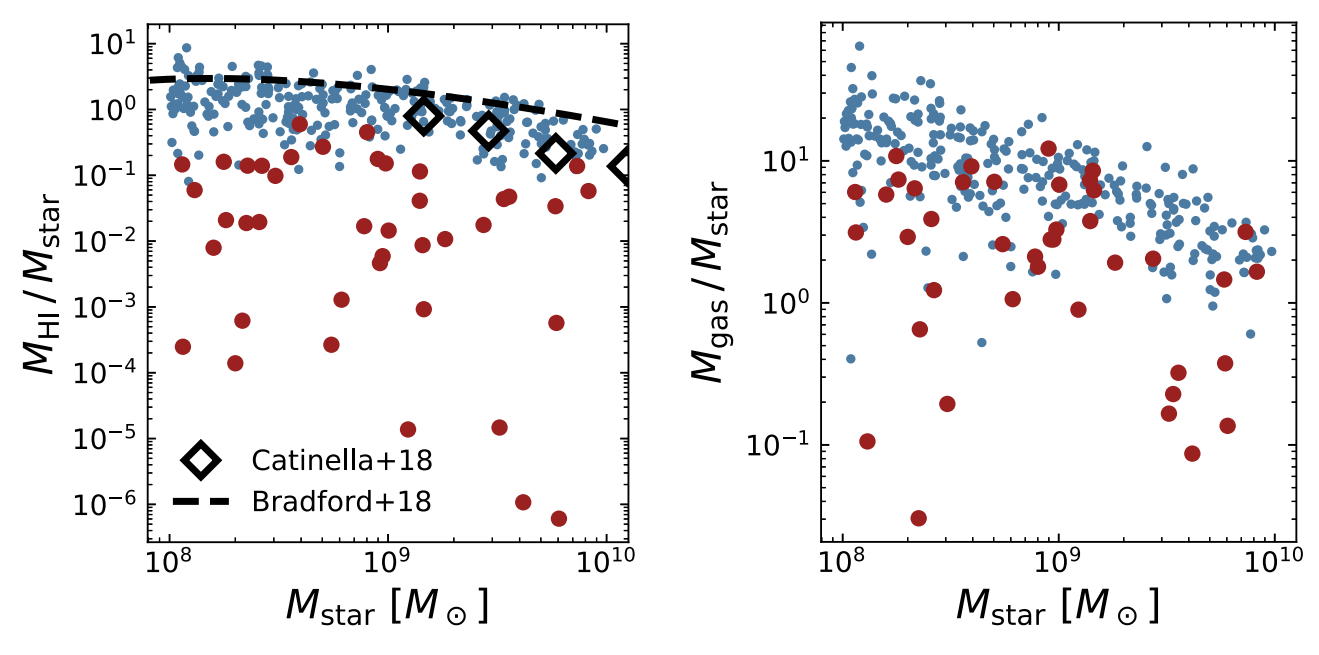


Figure 6. Fraction of gas to stars vs. stellar mass within quiescent dwarfs (red circles) and star-forming dwarfs (blue dots). Left: Fraction of H I gas to stellar mass, with observations from Catinella et al. (2018, black diamonds) and Bradford et al. (2018, black dashed) overplotted. Quiescent dwarfs contain orders of magnitude less H I gas at fixed stellar mass relative to star-forming dwarfs. Right: Fraction of total gas content to stellar mass. Quiescent dwarfs contain less cool, star-forming gas, and generally less gas overall relative to star-forming galaxies.

#### 3.3. Interactions Rarely Lead to Quenching

Before we can fully assess the impact of internal, MBH-driven processes on star formation, it is important to rule out the possibility of interactions driving the majority of quiescence. By selecting galaxies in isolation, we have mitigated (but not eliminated) the effects of environmental quenching on our dwarfs. We first ask how quenching compares among dwarfs in isolation relative to those with neighbors.

In Figure 7, we show the quiescent fraction at z=0.05 as a function of the distance to the nearest host,  $d_{\rm host}$ . As in Dickey et al. (2021), we separate galaxies into two stellar mass bins: just below the Geha et al. (2012) quenching threshold ( $10^{8.5} < M_{\rm star}/M_{\odot} < 10^9$ ), and just above ( $10^{9.5} < M_{\rm star}/M_{\odot} < 10^{10}$ ). As before, we show the median across all 25 sight lines and compare it with results from other cosmological simulations as well as SDSS observations.

Similar to other simulations, both quiescent isolated and quiescent nonisolated galaxies in ROMULUS25 are produced in excess relative to SDSS observations. In the higher mass bin, ROMULUS25, EAGLE, and SIMBA produce quiescent fractions consistent with SDSS for  $d_{\rm host} > 1.5$  Mpc, though most simulations slightly overproduce quiescent galaxies for  $d_{\rm host} < 1.5$  Mpc. In the lower mass bin, however, all simulations produce too many quiescent nonisolated galaxies, to varying degrees. In particular, ROMULUS25 yields nonisolated quiescent fractions between 20% and 30%, substantially higher than the 0%–10% found in SDSS. It is possible that the mechanism responsible for quenching isolated galaxies in the simulations also impacts quenching in dense environments and may explain the overproduction of low-mass quiescent dwarfs in dense environments.

We may also ask how quiescence varies for dwarfs with and without MBHs as a function of the environment. Figure 8 shows the quiescent fraction as a function of the distance to the nearest massive neighbor, distinguishing between dwarfs with

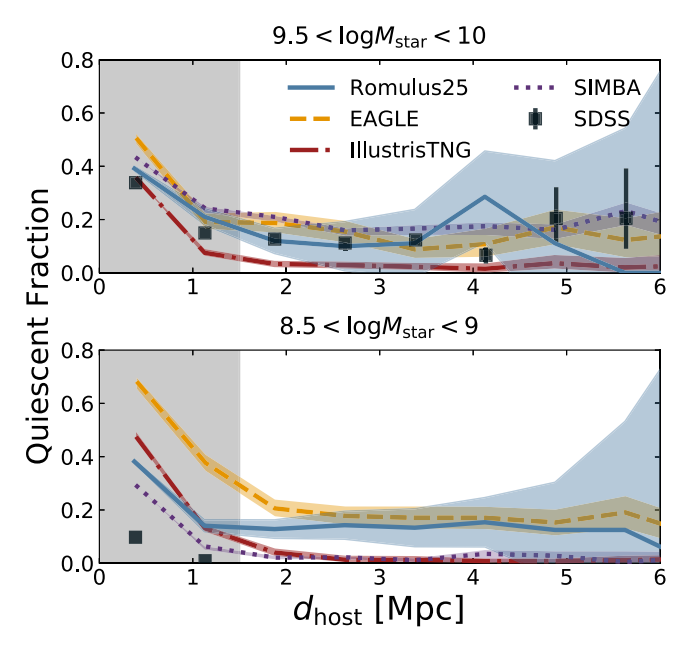


**Figure 7.** Quiescent fraction across 25 sight lines as a function of the distance from the nearest massive neighbor. Legend is as in Figure 2. For comparison with Dickey et al. (2021), we distinguish between high-mass dwarfs (top panel,  $10^{9.5} < M_{\rm star}/M_{\odot} < 10^{10}$ ) and low-mass dwarfs (bottom panel,  $10^{8.5} < M_{\rm star}/M_{\odot} < 10^{10}$ ). The black-shaded region indicates  $d_{\rm host} < 1.5$  Mpc, the threshold for galaxy isolation. ROMULUS25 dwarfs (isolated and nonisolated) exhibit the same trends as most other simulations, showing quiescent fractions in agreement with observations for high-mass dwarfs, but predicting too many quiescent low-mass dwarfs. At low masses, all simulations produce too many quiescent dwarfs even within group environments with  $d_{\rm host} < 1.5$  Mpc.

central MBHs and those without MBHs. As in Figure 7, we split high- and low-mass dwarfs.

High-mass dwarfs with central MBHs tend to follow observed quiescent fractions in both the group and field environments. High-mass dwarfs without MBHs follow observed quiescent fractions in group environments, though

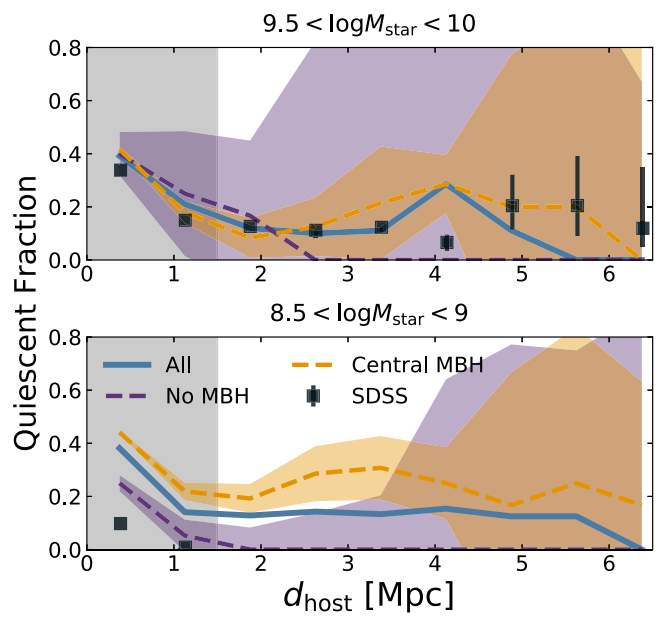


**Figure 8.** Quiescent fraction across 25 sight lines in ROMULUS25 as a function of the distance from the nearest massive neighbor, distinguishing between all dwarfs (blue), those with central MBHs (yellow), and those with no MBH (purple). As in Figure 7, we distinguish between high-mass dwarfs (top panel,  $10^{9.5} < M_{\rm star}/M_{\odot} < 10^{10}$ ) and low-mass dwarfs (bottom panel,  $10^{8.5} < M_{\rm star}/M_{\odot} < 10^{9}$ ). Uncertainties are omitted on the "All" line for clarity. The gray-shaded region marks  $d_{\rm host} < 1.5$  Mpc, the threshold for galaxy isolation. High-mass dwarfs with central MBHs are equally likely to be quenched in the field relative to those without MBHs. Low-mass ROMULUS25 dwarfs with central MBHs are more likely to be quenched in both the field and in groups, relative to those without MBHs. Dwarfs without MBHs in both mass ranges show closer agreement to observations of the quiescent fraction (Dickey et al. 2021, black squares).

drop more rapidly with  $d_{\rm host}$  than observations. On the other hand, low-mass dwarfs with central MBHs tend to overpredict the quiescent fraction in both the group and field environments. As seen earlier, dwarfs with central MBHs drive much of the discrepancy between ROMULUS25 and observed quiescent fractions, and indeed low-mass dwarfs without MBHs show much closer agreement with observations.

It is important to note that there are cases of splash back (e.g., Tinker et al. 2017) in our sample, where a galaxy that is currently isolated was within close proximity of a larger halo in the past. By tracing back each target halo's interaction history, we identify times when the target halo first fell within the radius of a more massive halo and compare these to the quenching times,  $t_{90}$ .

Overall, we find that splash back is unlikely to play a major role in quenching our dwarf galaxy sample. Of the 328 galaxies in our sample, 60 (20%) have undergone splash back in the past. Approximately 17% of splash-back galaxies are quiescent, only slightly higher than the 12% of no-splash-back galaxies that are quiescent. Conversely, 24% of quiescent galaxies are splash back, only slightly higher than the 17% of star-forming galaxies that are splash back. The number of splash-back galaxies is dependent on stellar mass, where dwarfs below  $M_{\rm star}/M_{\odot} < 10^9$  make up 77% of splash-back galaxies. Still, these lower-mass dwarfs show similar quiescent fractions between those that are splash back (17%) and no splash back (11%).

These splash-back results are in line with findings from recent zoom cosmological simulations, which have found that low-mass satellites ( $M_{\rm star}/M_{\odot}\lesssim 10^8$ ) continue forming stars for 2–5 Gyr after infall into the host halo (Akins et al. 2021), while higher-mass satellites ( $M_{\rm star}/M_{\odot}\gtrsim 10^8$ ) typically never fully quench (Akins et al. 2021; Samuel et al. 2022). While a small number of our isolated dwarfs likely quench due to splash back, the majority do not.

Finally, we determine whether mergers are the primary mode by which quiescence was catalyzed. Mergers are thought to dissipate gas angular momentum, channeling gas and driving quenching via a starburst (e.g., Wild et al. 2009, 2016) or AGN activity (e.g., Hopkins et al. 2006, 2008). We climb each target halo's merger tree backward in time in search of cases where the next, earlier snapshot contains more than one progenitor. We restrict our search to mergers with halo mass ratios >1:10 at the snapshot time. Identifying mergers in this way misses the effects of minor progenitors that become stripped over time but captures the effects of major mergers. The merger time,  $t_{\rm merge}$ , is then the cosmic time of the snapshot containing only the descendant of the merger. Following McAlpine et al. (2020), we define the dynamical time as the freefall time of a dark matter halo,

$$t_{\rm dyn} = \left(\frac{3\pi}{32G(200\rho_{\rm c})}\right)^{1/2},\tag{5}$$

where  $\rho_c$  is the critical density of the universe at time t. For reference,  $t_{\rm dyn} \sim 1.58$  Gyr at z=0.05. We identify dwarfs that underwent mergers within one dynamical time of the quenching time,  $|t_{\rm merge} - t_{90}| < t_{\rm dyn}$ .

Mergers are unlikely to be the primary mechanism by which quenching is initiated. Only 11% of quiescent dwarfs have undergone significant mergers within one dynamical time of  $t_{90}$ , similar to the 10% of star-forming dwarfs. Relaxing our criteria, we find that 21% of quiescent dwarfs have undergone a merger within two dynamical times of quenching, similar to the 18% of star-forming dwarfs. Evidently, mergers are not a hard requirement to initiate quenching of isolated dwarf galaxies.

#### 3.4. Internal Processes Can Quench Isolated Dwarfs

Turning now to the precise effects of feedback, we calculate the integrated energy injection from both MBHs and Type II supernovae (SNe II) into the surrounding ISM. There is precedent for exploring the underlying energetics of AGN in relation to quenching. Using high-resolution cosmological simulations of a  $M_{\rm vir}=10^{12}M_{\odot}$  halo, Pontzen et al. (2017) showed that galaxy quenching is related to a greater contribution from MBH activity to the total energy injected. Similarly, Dashyan et al. (2018) use analytic models of AGN energetics to show that large regions of the AGN efficiency—lifetime parameter space in dwarf galaxies are more favorable to AGN-driven gas removal versus SNe-driven removal.

Dashyan et al. (2018) use analytic models to show that feedback from AGN may be even more successful than SNe in driving out gas from galaxies below a critical halo mass threshold.

Within ROMULUS25, the integrated energy injected into the surrounding gas by SNe II is directly related to the number of SNe II that have detonated within the galaxy,  $N_{\rm SN}$ . Although other types of SNe are implemented, we ignore the effects of Type Ia SNe as they do not drive large-scale blast-wave feedback in ROMULUS25 (Stinson et al. 2006). As the timing of

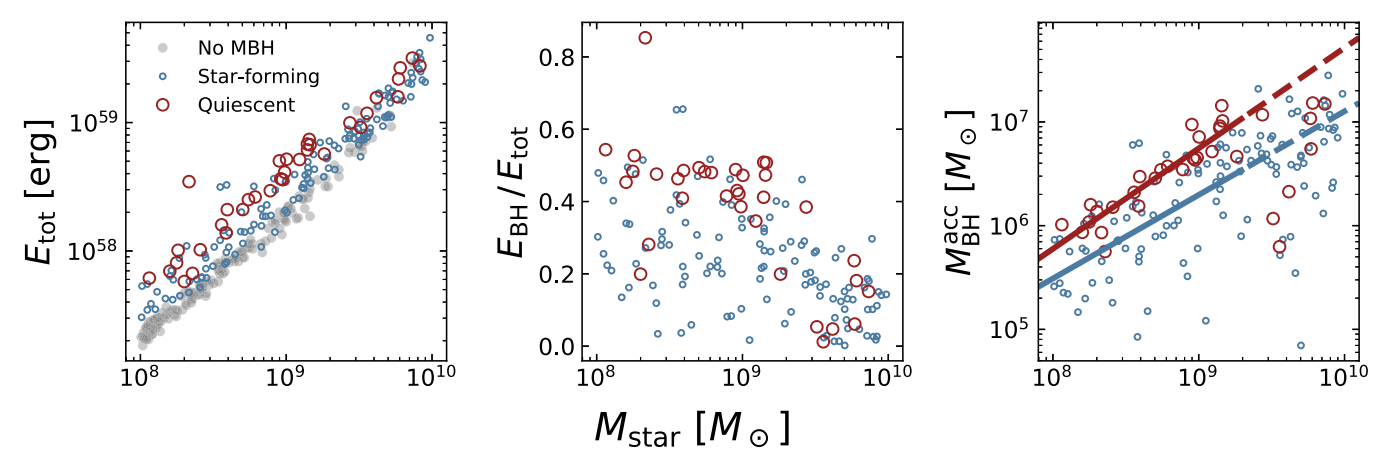


Figure 9. Left: total energy injection from MBHs and SNe as a function of the stellar mass for star-forming dwarfs with central MBHs (blue unfilled dots), quiescent dwarfs with central MBHs (red unfilled circles), and dwarfs entirely without MBHs (gray filled circles). Middle: fraction of energy injection contributed by MBHs as a function of the stellar mass for dwarfs with central MBHs. Quiescent dwarfs below  $M_{\text{star}}/M_{\odot} < 2 \times 10^9$  tend to have higher amounts of total energy injection at fixed stellar mass, and more of this energy injection tends to come from MBHs. Dwarfs above  $M_{\text{star}}/M_{\odot} > 2 \times 10^9$  have similar amounts of total energy injection, in line with simulation results from Pontzen et al. (2017). Only a small fraction of dwarfs are entirely dominated by energy injection from the MBH. Right:  $M_{\text{BH}}^{\text{acc}} - M_{\text{star}}$  relation for quiescent and star-forming dwarfs with central MBHs. We fit the relation below  $M_{\text{star}}/M_{\odot} < 2 \times 10^9$  for quiescent galaxies (red solid) and star-forming galaxies (blue solid), showing the extrapolated fits with dashed lines.

the SNe II depends on the mass of the stellar progenitor, integrating over the IMF provides the number of stars that will explode within a given star particle, where only stars between 8 and 40  $M_{\odot}$  are allowed to detonate as SNe II (Stinson et al. 2006). Each SNe II event injects the same amount of energy into the surrounding gas,  $dE_{\rm SN} = 0.75 \times 10^{51}\,\rm erg$  (Tremmel et al. 2017). The integrated SNe energy injection can then be written:

$$E_{\rm SN} = N_{\rm SN} dE_{\rm SN}. \tag{6}$$

The energy injected by the MBH into the surrounding ISM is directly related to the accretion rate,  $\dot{M}$ , via the radiative efficiency,  $\epsilon_{\rm r}=0.1$ , and the gas coupling efficiency,  $\epsilon_{\rm f}=0.02$  (Tremmel et al. 2017). The integrated MBH energy injection can then be written:

$$E_{\rm BH} = \epsilon_{\rm r} \, \epsilon_{\rm f} \dot{M} c^2 dt, \tag{7}$$

where the accretion is assumed to be constant throughout one MBH simulation time step, dt.

The left panel of Figure 9 shows the total energy injected into each dwarf's ISM,  $E_{\rm tot} = E_{\rm BH} + E_{\rm SN}$ , as a function of the stellar mass, where we distinguish between quiescent and star-forming dwarfs with central MBHs, and dwarfs entirely without MBHs. As the number of SNe II events scales directly with the number of star particles,  $E_{\rm SN}$  is closely tied to the stellar mass of the galaxy. Hence at a fixed stellar mass, the difference between dwarfs without MBHs and those with central MBHs is largely due to energy injection from the MBH.

The MBH energy injection is seen in more detail in the center panel of Figure 9, where we instead show the fractional contributions of MBHs to the total energy injected,  $(E_{\rm BH})/(E_{\rm BH}+E_{\rm SN})$ . Here, we only include dwarfs with central MBHs. Among dwarfs with  $M_{\rm star}/M_{\odot} < 2 \times 10^9$ , the fraction of the energy budget attributable to MBHs is higher in quiescent dwarfs than in star-forming dwarfs. Above  $M_{\rm star}/M_{\odot} > 2 \times 10^9$ , dwarfs shift to strongly SNe-dominated, with little difference in the energy injection between quiescent and star-forming galaxies.

The latter behavior is slightly different from results of Pontzen et al. (2017), who study cosmological simulations of a  $M_{\rm vir} = 10^{12} M_{\odot}$  halo at z = 2. They find that the total energy injection from feedback is comparable between MBHs+SNe runs and SNe-only runs of their halo, despite quenching only occurring in the MBH+SNe runs. However, they find that  $E_{\rm BH} > E_{\rm SN}$  in cases where the halo quenches. In contrast, our lower-mass dwarfs with MBHs have slightly enhanced  $E_{tot}$ , and only 15% of all quiescent dwarfs and 3% of all star-forming dwarfs exhibit  $E_{\rm BH} > E_{\rm SN}$ . Evidently, MBHs only need to contribute a significant amount of energy in order to quench, and do not necessarily need to dominate the energy budget. The importance of MBH energy injection in suppressing star formation is in agreement with results from Piotrowska et al. (2022), who study the quenching mechanisms  $M_{\rm star} > 10^9 M_{\odot}$  central galaxies in the EAGLE, ILLUSTRIS, and ILLUSTRISTNG cosmological simulations. Using a random forest classifier, they find that classification of a galaxy as starforming or quiescent is most closely tied to the integrated accretion history of the central MBH. However, as discussed in Section 3.1, the other simulations considered in this work do not seed MBHs in galaxies below  $M_{\rm star} < 10^9 M_{\odot}$ . Dickey et al. (2021) find that the overproduction of low-mass quenched dwarfs in these other simulations is instead due to either environmental effects, feedback from SNe, or outflows from nearby massive galaxies.

As discussed above, the energy injection from SNe II and MBHs are closely related to the stellar mass and accreted MBH mass, respectively. The right panel of Figure 9 shows the  $M_{\rm BH}^{\rm acc}-M_{\rm star}$  relation for our isolated dwarf sample with central MBHs. Linear fits to the  $M_{\rm BH}^{\rm acc}-M_{\rm star}$  relation for quiescent and star-forming galaxies below  $M_{\rm star}/M_{\odot} < 2 \times 10^9$  indicate that quiescent dwarfs host MBHs  $3\times$  more massive than the MBHs in corresponding star-forming dwarfs. This phenomenon is directly in line with results from Sharma et al. (2020), which found that overmassive MBHs are related to star formation suppression and gas depletion in ROMULUS25 dwarf galaxies. However, this behavior breaks down for galaxies above  $M_{\rm star}/M_{\odot} > 2 \times 10^9$ , where three quiescent galaxies in fact

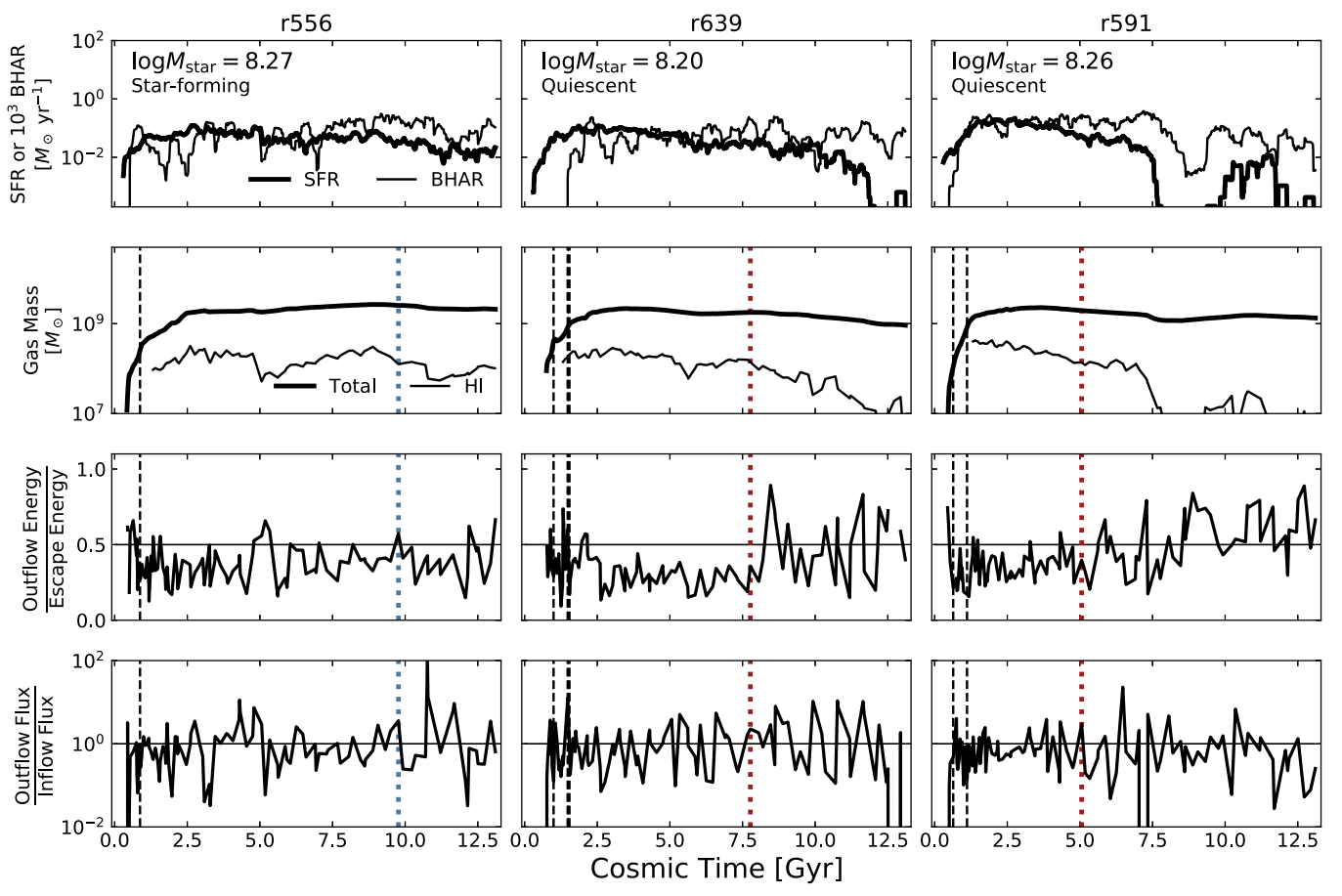


Figure 10. History of gas kinematics, star formation, and MBH accretion for three low-mass dwarf galaxies between  $10^8 < M_{\rm star}/M_\odot < 10^{8.3}$ , with one star-forming dwarf (left) and two quiescent dwarfs (center+right). We trace the properties of the most massive MBH within 2 kpc of the halo center. Each column is labeled with the internal halo number from ROMULUS25. All panels except the top row include vertical lines marking  $t_{90}$  (blue dotted for star-forming, red dotted for quiescent), as well as vertical lines marking mergers (dashed black; see Section 3.3 for details). *Ist row*: SFR (solid thick) and  $10^3 \times BHAR$  (solid thin) vs. cosmic time. *2nd row*: sSFR for the target halo normalized to the median sSFR at the corresponding epoch, across star-forming galaxies between  $10^8 < M_{\rm star}/M_\odot < 10^{8.3}$ . *3rd row*: Mass held within all gas particles (solid thick) and mass held within the H I component of gas particles (solid thin). *4th row*: Ratio of energy in outflowing gas at  $0.1 \times R_{200}$ , to the energy required to escape the potential from  $0.1 \times R_{200}$ . For clarity, the horizontal line (solid thin) marks the 0.5 threshold. *5th row*: Ratio of mass flux in outflowing gas at  $0.1 \times R_{200}$ .

host undermassive MBHs. The quenching mechanism for dwarfs above and below  $M_{\rm star}/M_{\odot}=2\times10^9$  clearly differ and will require closer inspection.

## 3.5. Case Studies

We now more closely examine the histories of gas mass, star formation, and MBH accretion for nine dwarfs as a way to understand the differences in quenching mechanisms. We divide our stellar mass range of interest into three bins,  $M_{\rm star} = [10^{8-8.3} M_{\odot}, \ 10^{8.8-9.2} M_{\odot}, \ 10^{9.7-10} M_{\odot}]$ , and randomly select one star-forming dwarf from each bin. For each star-forming galaxy, we select two quiescent galaxies with stellar masses within 0.1 dex.

For each dwarf at z=0.05, we trace the main halo progenitor backward in time through all available simulation snapshots. At each snapshot we record: the mass held within gas particles as well as the mass within the H I component; the inflowing/outflowing mass flux and energy of gas flowing across a 1 kpc thick shell of radius  $0.1 \times R_{200}$ ; and the energy required for gas to escape the gravitational potential from  $0.1 \times R_{200}$  out to  $R_{200}$ . We also identify the total SFR for the stars within the dwarf at

z=0.05, and the accretion rate of the central MBH, which are output at finer time resolution. These quantities may yield insight into how the timing of MBH activity affects the gas kinematics and ultimately star formation.

Studies connecting outflows and quenching within simulations have been done in the past. Pontzen et al. (2017) and Sanchez et al. (2021) study the properties of AGN outflows in massive galaxies, finding a strong connection between energetic outflows and galaxy quenching. Within the galaxy cluster environment, Tremmel et al. (2019) and Chadayammuri et al. (2021) find that large-scale, AGN-driven outflows regulate gas cooling onto the brightest cluster galaxy, quenching star formation. Koudmani et al. (2021) use the FABLE cosmological simulations to show that dwarf galaxies with energetic, MBH-driven outflows tend to exhibit reduced gas mass fractions and contribute to dwarf quenching at high redshift.

Figures 10–12 show case studies for dwarfs in each of the three mass bins. In each figure, the top row traces the SFR and  $10^3 \times MBH$  accretion rate across time. The second row traces the total gas mass and H I gas mass across time. The third row tracks the ratio of outflow gas energy to the escape energy

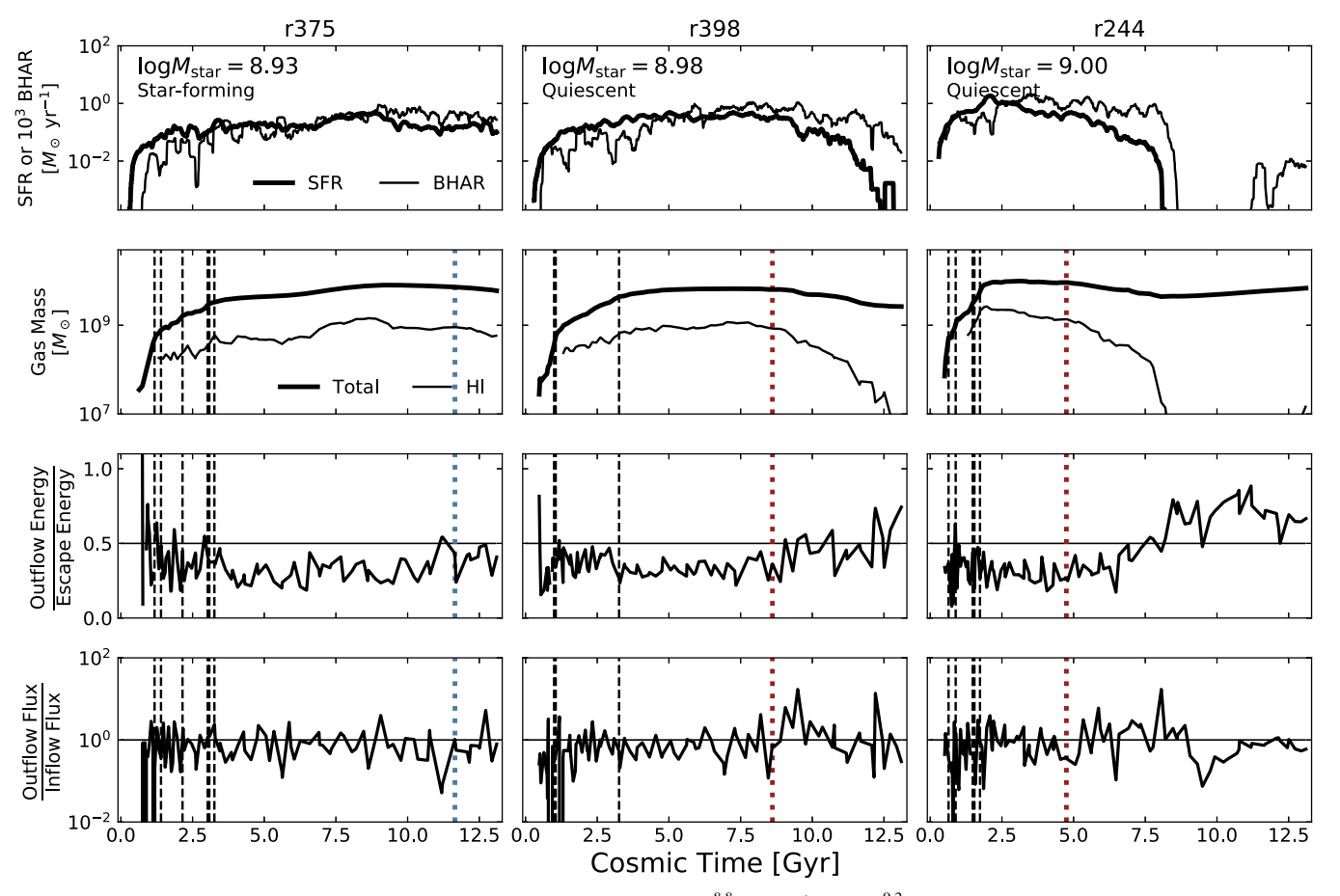


Figure 11. As in Figure 10, but for three intermediate-mass dwarf galaxies between  $10^{8.8} < M_{\rm star}/M_{\odot} < 10^{9.2}$ . Quenching can occur both slowly as in lower-mass dwarfs, or rapidly as in higher-mass dwarfs.

(Pontzen et al. 2017), where we define the outflow energy:

Outflow energy = 
$$\frac{\sum_{i} m_{i} v_{r,i} (u_{i} + v_{r,i}^{2}/2)}{\sum_{i} m_{i} v_{r,i}},$$
 (8)

where  $m_i$  is the gas particle mass,  $u_i$  is the gas internal energy, and  $v_{r,i}$  is the gas radial velocity. We also define the escape energy:

Escape energy = 
$$\Phi(R_{200}) - \Phi(0.1 \times R_{200})$$
, (9)

for spherically averaged potential,  $\Phi(r)$  at radius r.

Dwarfs at low masses  $(M_{\rm star} \sim 10^8 M_{\odot})$  quench slowly over several Gyr. The supply of star-forming gas is slowly used up or heated by both the central MBH and star formation. Although the outflow energetics indicate a quick increase in outflow energy following quenching, there are no coherent outflows that consistently drive gas outward across this radius. Further, H I mass decreases over time while the total gas mass remains constant or slowly decreases, suggesting that the quenching mechanism struggles to physically remove gas but can suppress cooling. Along with the fact that MBH activity continues after quenching, together these suggest that quenching for low-mass dwarfs is driven by gas heating induced by the combination of star formation and MBH activity. The quenched status is maintained by continued MBH feedback. At early times, the galaxy is able to accrete and cool gas, allowing star formation and MBH accretion to proceed until the point that heating from the MBH overwhelms ISM cooling.

Dwarfs at high masses instead quench explosively (see Figure 12), similar to what is thought to occur in more massive galaxies (Hopkins et al. 2005; Ishibashi & Fabian 2016). Highmass dwarfs tend to quench within a short period of time (<1 Gyr), with a period of rapid gas inflow driving fast MBH accretion, which in turn heats up gas and drives it outward across  $0.1 \times R_{200}$ . In the case of r123, both MBH accretion and star formation drop quickly but maintain low levels. Star formation in r126 instead drops and stays at zero at the time of quenching, while the MBH continues to accrete at low levels. In both cases, nearly all of the gas is swept up and driven outside of  $0.1 \times R_{200}$ . However, the outflow energies indicate the gas is not able to fully escape the halo, and instead it is kept hot in the outskirts of the halo. The impact of the central MBH on the outskirts of the halo is in stark contrast with zoom simulation results from Sanchez et al. (2019, 2021), which find that MBHs in Milky Way–mass halos can drive large outflows from the disk but are not able to drive changes in gas content in the circumgalactic medium. They find that MBH-induced outflows are able to transport metals to the outskirts, but do not strongly impact the temperature and densities of gas far from the halo center.

Dwarfs at intermediate masses make up a middle ground between slow and fast quenching (see Figure 11); Both r398 and r244 quench more rapidly than the lower-mass dwarfs, steadily declining in sSFR over the 3 Gyr following the  $t_{90}$  point, until shutting off star formation completely. The quenching in r244 is also mirrored in the shutoff of MBH accretion around the same time. These dwarfs may exist at a critical mass where quenching changes from the explosive

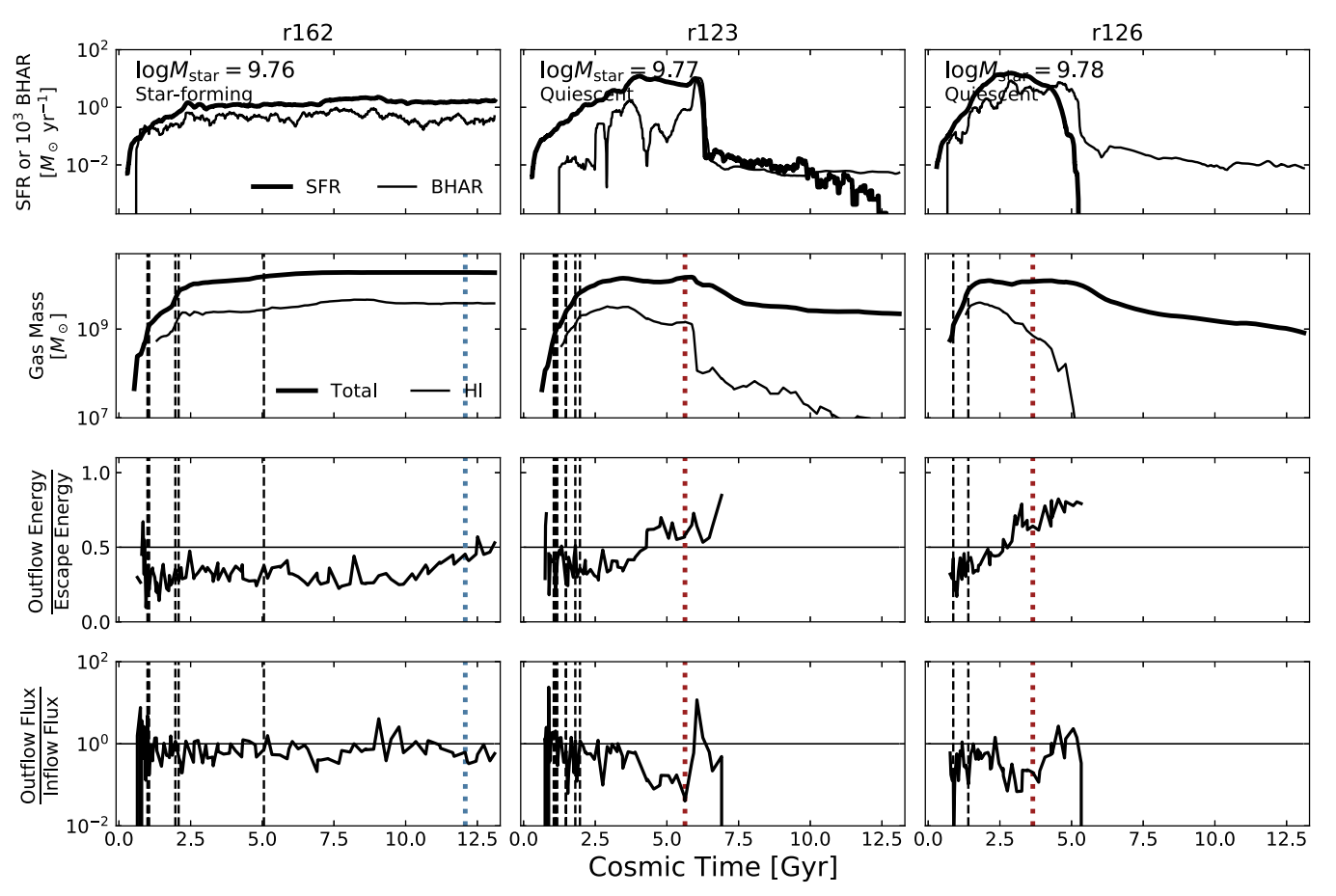


Figure 12. As in Figure 10, but for three high-mass dwarf galaxies between  $10^{9.7} < M_{\text{star}}/M_{\odot} < 10^{10}$ . Quenching occurs rapidly in a "blowout" phase, in stark contrast to the slow quenching found in lower-mass dwarfs. Outflows within r123 and r126 shutdown within 1 Gyr of  $t_{90}$ , causing a truncation in the energy and flux panels.

"blowouts" found among massive galaxies to the slow heating found in lower-mass dwarfs.

Note that in all of these mass bins, the star-forming cases also contain an MBH. Although hosting a central MBH is typically necessary to quench a dwarf galaxy in these simulations, it is not alone sufficient in order to quench. The MBH needs to be hosted within an environment where it can accrete efficiently. In lower-mass dwarfs, the MBH must undergo sustained accretion for long periods of time. To get complete quenching in higher-mass dwarfs, the MBH must rapidly accrete a large amount of gas. Although mergers might help in funneling large amounts of gas toward the galaxy center, mergers are not necessary for driving quenching, even among these higher-mass dwarfs.

Overall, these trends give insight into how our dwarf galaxies stop forming stars. Gas that may otherwise form stars is instead kept hot and/or completely driven out while replenishing inflows of cold gas from the circumgalactic and intergalactic medium are suppressed. This combination of gas "starvation" (Peng et al. 2015) and gas depletion is reminiscent of the mechanisms invoked in recent studies to explain quenching in local low-mass galaxies. Trussler et al. (2020) study the chemical properties of optically selected local galaxies with stellar masses  $M_{\rm star} > 10^9 M_{\odot}$ , showing that passive star formation in their sample is likely driven by a combination of gas starvation and *ejection* via outflows. Bluck et al. (2020) similarly train a neural network on spatially resolved spectroscopic observations of 3500 local  $M_{\rm star} > 10^9 M_{\odot}$  galaxies from MaNGA (Aguado et al. 2019), showing that global properties of central galaxies (e.g., central velocity dispersion) are more

powerful predictors of spaxel-wise quiescence than even spaxel-wise properties (e.g., stellar mass surface density per IFU spaxel). They find that galaxy-wide gas starvation and MBH feedback are the primary sources of quenching among central galaxies.

## 4. Discussion

As discussed in Sharma et al. (2020), the primary caveat when analyzing MBHs in ROMULUS25 is the large seed mass of MBHs ( $10^6\ M_{\odot}$ ) relative to analytic estimates for direct-collapse seeding (Haiman 2013). MBHs are seeded at these relatively large masses to better resolve their dynamics within the simulation (Tremmel et al. 2017). However, the Bondi–Hoyle accretion prescription scales with MBH mass, which, if the MBH mass is already overly large to begin with, may drive unrealistic accretion onto the MBH. Indeed, Sharma et al. (2020) finds that overmassive MBHs in ROMULUS25 tend to lie at higher masses than expected from observational constraints of the  $M_{\rm BH}$ – $M_{\rm star}$  relation.

Similarly, the Bondi–Hoyle accretion prescription, which appears to work for massive galaxies, may not apply to low-mass galaxies. Sharma et al. (2022) find that ROMULUS25 is able to reproduce observed relationships between the AGN luminosity, SFR, and stellar mass among dwarf AGN, but the simulation also produces too many bright dwarf AGN relative to observations. Instead, a two-mode accretion model (Churazov et al. 2005) with a dependence on mass or Eddington fraction that allows for similar amounts of growth

but with a lower seed mass may better match observations of the AGN fraction.

In this work, we push down to the lowest resolvable scales in ROMULUS25 in order to capture both MBH physics and quenching physics in dwarf galaxies. It is possible that our results are affected by numerics at the lowest dwarf masses, where the lower resolutions lead to fluffier, low-resolution gas that is more susceptible to feedback. Note, however, that related analyses by Dickey et al. (2021) indicate that resolution effects may not fully explain the discrepancy in quiescent fractions between simulations and observations below  $M_{\rm star}/M_{\odot} = 10^9$ . They find the discrepancy in quiescent fraction compared to observations is still present when recalculating their results for the smaller, higherresolution runs of EAGLE (moving from the 100 Mpc to the 25 Mpc boxes) and SIMBA (moving from the 100 Mpc to the 25 Mpc box). Depending on the simulation, moving to higherresolution runs either decreased or increased the discrepancy, but never eliminated it. It is hence also possible that running higher resolutions of ROMULUS25 would still not solve the discrepancy in quiescent fractions.

Similarly, ROMULUS25 does not simulate  $H_2$  gas physics—all SFRs in this work are based solely on the temperature, density, and metallicity of the gas particles. By resimulating a cosmological volume of dwarf galaxies at higher resolution, Munshi et al. (2019) find that the introduction of  $H_2$  gas physics (including  $H_2$  shielding and photodissociation via Lyman–Werner radiation) can strongly impact the star formation properties of low-mass halos. Introducing  $H_2$  serves to delay the onset of star formation in halos with  $M_{\rm vir} < 10^9 M_{\odot}$ , leading to a reduction in galaxy stellar masses and a reduction in the number of halos that form stars. In the case of dwarf galaxies in ROMULUS25, the precise impact of  $H_2$  physics on star formation is not known, though it is likely that SFRs would diminish, leading to *higher* quiescent fractions.

As discussed in Ricarte et al. (2019), ROMULUS25 is one of several state-of-the-art cosmological simulations which have found that mergers are not the primary mode by which low- and intermediate-luminosity AGN are triggered (Martin et al. 2018; McAlpine et al. 2018, 2020; Steinborn et al. 2018). Results for ROMULUS25 indicate that quenching progresses through sustained growth of the stellar and MBH components. However, high-resolution simulations suggest that MBH assembly may depend dramatically on resolution (Anglés-Alcázar et al. 2017)—ROMULUS25 may not resolve MBH accretion of small-scale, high-density gas brought in through mergers. Higher-resolution zoom cosmological simulations may be required to fully disentangle the effects of numerics on MBH growth through mergers, MBH feedback, and dwarf galaxy quenching.

All in all, it is likely that the AGN in ROMULUS25 overinfluence isolated dwarf galaxies via accreting too readily and coupling too closely to the ISM. While ROMULUS25 can reproduce observed local scaling relations, the resolution and/or physical prescriptions likely do not capture the true nature of accretion and feedback in low-mass galaxies. On the other hand, as shown in Dickey et al. (2021), other cosmological simulations without MBHs in  $M_{\rm star} < 10^9 M_{\odot}$  dwarfs still exhibit an overabundance of isolated, quenched dwarfs. Further confusing the picture is deep optical imaging from Prole et al. (2020), which indicates the quiescent fraction among isolated, low-surface-brightness galaxies may in fact agree with cosmological simulations. If the true quiescent fraction is indeed as high as their imaging indicates, then our work sets a

strong precedent for future searches of MBH activity in these isolated, quiescent, low-surface-brightness galaxies.

Evidently, there is a need for (1) higher-resolution simulations with an emphasis on MBH growth and feedback in the lowest-mass galaxies, (2) further deep imaging constraining the quiescent fraction for low-surface-brightness galaxies unlikely to be captured by large-scale surveys, and (3) constraints on the presence of MBHs in any known isolated, quiescent dwarfs.

#### 5. Conclusion

We analyze quenching among isolated dwarf galaxies in the ROMULUS25 cosmological hydrodynamic simulation, which uniquely seeds MBHs in resolved, low-mass galaxies in the early universe. Using the mock-observation package *orchard*, we generate mock sight lines through the simulation box in order to measure quiescence as an observer would define it. This method allows us to make direct comparisons with observations and other mock-observed simulations from Dickey et al. (2019). We find that:

- 1. Similar to other large-scale cosmological simulations, ROMULUS25 predicts a greater number of isolated, quiescent dwarfs with stellar masses below  $M_{\rm star}/M_{\odot} < 2 \times 10^9$  at z=0.05 than is observed in SDSS (Figure 2). As seen in Figure 3, this discrepancy can be explained by the presence of dwarfs with central MBHs, which exhibit 2–10 times higher quiescent fractions relative to dwarfs without MBHs. On the other hand, deep optical imaging (Prole et al. 2020) places the quiescent fraction around  $\sim 26\%$ , similar to the fractions found in cosmological simulations.
- 2. Quiescent dwarfs form their stars and then quench around  $z \sim 0.5-1$ , as seen in Figure 4, though the precise quenching time depends on stellar mass.
- 3. Quenching is strongly associated with energy injection into the ISM by MBHs, as seen in Figure 9. Figures 4 and 6 indicate that, by z=0.05, quiescent dwarfs have significantly less HI gas, as well as less total gas, than star-forming dwarfs. Quiescent dwarf galaxies are more likely to host an MBH that has accreted more mass over cosmic time, thereby releasing more energy in the form of AGN feedback.
- 4. Dwarf galaxies across two dex in stellar mass quench at the onset of energetic black hole outflows, similar to what is seen in more massive galaxies (Pontzen et al. 2017; Tremmel et al. 2019; Sanchez et al. 2021). The most massive dwarfs in our sample ( $M_{\rm star}=10^{9.3}-10^{10}~M_{\odot}$ ) experience rapid blowout events that significantly decrease the overall gas content of the halo. Lower-mass dwarfs (below  $\sim 10^{9.3}~M_{\odot}$ ), on the other hand, experience a more gradual quenching process with continuous black hole activity and outflows with less extreme changes to their halo gas content.

Our simulated dwarf galaxies, along with a slew of recent observational results (e.g., Silk 2017; Bradford et al. 2018; Penny et al. 2018; Dickey et al. 2019; Manzano-King et al. 2019), support the idea that AGN feedback may be an important ingredient to dwarf galaxy evolution. It is likely that a large number of dwarfs host an MBH (e.g., Baldassare et al. 2020), and it is already known that dwarf galaxies can be an important laboratory to constrain MBH formation (Volonteri & Natarajan 2009; Greene 2012; Volonteri 2012).

In this work we showed the crucial impact of MBHs in creating a population of quenched, isolated dwarf galaxies. This demonstrates that low-mass galaxies may also provide crucial constraints on the nature of AGN feedback. Modern cosmological simulations include a variety of different models for AGN feedback, yet these models are often created and optimized with massive galaxies in mind. The ability to model MBHs in dwarf galaxies and test against observations at low mass can provide a new way to constrain these models. Higher-resolution simulations, which we will perform in future work, will provide even more insight into the detailed interactions between MBHs and the ISM of dwarf galaxies while new implementations of AGN feedback will be tested against observed dwarfs, as well as high-mass galaxies.

## Acknowledgments

This material is based on work supported by the National Science Foundation under grant No. NSF-AST-1813871. M.T. is supported by an NSF Astronomy and Astrophysics Postdoctoral Fellowship under award AST-2001810. J.M.B. acknowledges support from NSF-AST-1812642. ROMULUS25 is part of the Blue Waters sustained-petascale computing project, which is supported by the National Science Foundation (awards OCI-0725070 and ACI-1238993) and the state of Illinois. Blue Waters is a joint effort of the University of Illinois at Urbana-Champaign and its National Center for Supercomputing Applications. ROMULUS25 initial conditions and preliminary analysis used the Extreme Science and Engineering Discovery Environment (XSEDE), which is supported by National Science Foundation grant No. ACI-1548562. R.S.S. would like to thank Nicole Sanchez, Claire Dickey, and Tjitske Starkenburg for helpful conversations and data from private communications. We thank the anonymous referee for the insightful feedback that improved this manuscript.

## **ORCID** iDs

```
References
Aguado, D. S., Ahumada, R., Almeida, A., et al. 2019, ApJS, 240, 23
Akins, H. B., Christensen, C. R., Brooks, A. M., et al. 2021, ApJ, 909, 139
Anglés-Alcázar, D., Faucher-Giguère, C. A., Quataert, E., et al. 2017, MNRAS
   Lett., 472, L109
Applebaum, E., Brooks, A. M., Christensen, C. R., et al. 2021, ApJ, 906, 96
Bahé, Y. M., & McCarthy, I. G. 2015, MNRAS, 447, 969
Baldassare, V. F., Geha, M., & Greene, J. 2020, ApJ, 896, 10
Baldry, I. K., Balogh, M. L., Bower, R. G., et al. 2006, MNRAS, 373, 469
Baldry, I. K., Glazebrook, K., Brinkmann, J., et al. 2004, ApJ, 600, 681
Balogh, M. L., Baldry, I. K., Nichol, R., et al. 2004, ApJL, 615, L101
Balogh, M. L., Morris, S. L., Yee, H. K. C., Carlberg, R. G., & Ellingson, E.
   1999, ApJ, 527, 54
Barai, P., & de Gouveia Dal Pino, E. M. 2019, MNRAS, 487, 5549
Begelman, M. C., Volonteri, M., & Rees, M. J. 2006, MNRAS, 370, 289
Bell, E. F., McIntosh, D. H., Katz, N., & Weinberg, M. D. 2003, ApJS,
   149, 289
Bellovary, J. M., Cleary, C. E., Munshi, F., et al. 2019, MNRAS, 482, 2913
Bettinelli, M., Hidalgo, S. L., Cassisi, S., Aparicio, A., & Piotto, G. 2018,
Binney, J., & Tabor, G. 1995, MNRAS, 276, 663
Blanton, M. R., Kazin, E., Muna, D., Weaver, B. A., & Price-Whelan, A. 2011,
```

AJ, 142, 31

```
Bluck, A. F. L., Maiolino, R., Piotrowska, J. M., et al. 2020, MNRAS,
   499, 230
Bower, R. G., Benson, A. J., Malbon, R., et al. 2006, MNRAS, 370, 645
Bradford, J. D., Geha, M. C., Greene, J. E., Reines, A. E., & Dickey, C. M.
  2018. ApJ. 861, 50
Brammer, G. B., Whitaker, K. E., van Dokkum, P. G., et al. 2009, ApJL,
   706, L173
Brinchmann, J., Charlot, S., White, S. D. M., et al. 2004, MNRAS, 351, 1151
Brown, T., Catinella, B., Cortese, L., et al. 2015, MNRAS, 452, 2479
Brown, T. M., Tumlinson, J., Geha, M., et al. 2014, ApJ, 796, 91
Byler, N., Dalcanton, J. J., Conroy, C., & Johnson, B. D. 2017, ApJ, 840, 44
Cannon, J. M., Giovanelli, R., Haynes, M. P., et al. 2011, ApJL, 739, L22
Cassata, P., Cimatti, A., Kurk, J., et al. 2008, A&A, 483, L39
Catinella, B., Saintonge, A., Janowiecki, S., et al. 2018, MNRAS, 476, 875
Cattaneo, A., Dekel, A., Faber, S. M., & Guiderdoni, B. 2008, MNRAS,
   389, 567
Chabrier, G. 2003, PASP, 115, 763
Chadayammuri, U., Tremmel, M., Nagai, D., Babul, A., & Quinn, T. 2021,
   MNRAS, 504, 3922
Charlot, S., & Fall, S. M. 2000, ApJ, 539, 718
Choi, E., Ostriker, J. P., Naab, T., Oser, L., & Moster, B. P. 2015, MNRAS,
   449, 4105
Choi, E., Somerville, R. S., Ostriker, J. P., Naab, T., & Hirschmann, M. 2018,
   ApJ, 866, 91
Churazov, E., Sazonov, S., Sunyaev, R., et al. 2005, MNRAS, 363, L91
Conroy, C., & Gunn, J. E. 2010, ApJ, 712, 833
Conroy, C., Gunn, J. E., & White, M. 2009, ApJ, 699, 486
Croton, D. J., Springel, V., White, S. D. M., et al. 2006, MNRAS, 365, 11
Dashyan, G., Silk, J., Mamon, G. A., Dubois, Y., & Hartwig, T. 2018,
         S. 473, 5698
Davé, R., Anglés-Alcázar, D., Narayanan, D., et al. 2019, MNRAS, 486, 2827
Davies, J. J., Pontzen, A., & Crain, R. A. 2022, MNRAS, 515, 1430
Dekel, A., & Silk, J. 1986, ApJ, 303, 39
Di Matteo, T., Springel, V., & Hernquist, L. 2005, Natur, 433, 604
Dickey, C. M., Geha, M., Wetzel, A., & El-Badry, K. 2019, ApJ, 884, 180
Dickey, C. M., Starkenburg, T. K., Geha, M., et al. 2021, ApJ, 915, 53
Efstathiou, G. 1992, MNRAS, 256, 43P
Emerick, A., Mac Low, M.-M., Grcevich, J., & Gatto, A. 2016, ApJ, 826, 148
Feldmann, R., Carollo, C. M., Mayer, L., et al. 2010, ApJ, 709, 218
Feldmann, R., Quataert, E., Hopkins, P. F., Faucher-Giguère, C.-A., &
   Kereš, D. 2017, MNRAS, 470, 1050
Fitts, A., Boylan-Kolchin, M., Elbert, O. D., et al. 2017, MNRAS, 471, 3547
Font, A. S., Bower, R. G., McCarthy, I. G., et al. 2008, MNRAS, 389, 1619
Foreman-Mackey, D., Sick, J., & Johnson, B. 2014, python-fsps: Python
   bindings to FSPS (v0.1.1) v0.1.1, Zenodo, doi:10.5281/zenodo.12157
Gallazzi, A., Brinchmann, J., Charlot, S., & White, S. D. M. 2008, MNRAS,
   383, 1439
Geha, M., Blanton, M. R., Yan, R., & Tinker, J. L. 2012, ApJ, 757, 85
Giallongo, E., Salimbeni, S., Menci, N., et al. 2005, ApJ, 622, 116
Giovanelli, R., Haynes, M. P., Kent, B. R., et al. 2005, AJ, 130, 2598
Governato, F., Weisz, D., Pontzen, A., et al. 2015, MNRAS, 448, 792
Greene, J. E. 2012, NatCo, 3, 1304
Greene, J. E., Strader, J., & Ho, L. C. 2020, ARA&A, 58, 257
Guedes, J., Callegari, S., Madau, P., & Mayer, L. 2011, ApJ, 742, 76
Habouzit, M., Volonteri, M., & Dubois, Y. 2017, MNRAS, 468, 3935
Hahn, C., Starkenburg, T. K., Choi, E., et al. 2019, ApJ, 872, 160
Haiman, Z. 2013, The First Galaxies, Vol. 396 (Berlin: Springer), 293
Haynes, M. P., Giovanelli, R., Martin, A. M., et al. 2011, AJ, 142, 170
Hidalgo, S. L., Aparicio, A., Skillman, E., et al. 2011, ApJ, 730, 14
Hirschmann, M., Dolag, K., Saro, A., et al. 2014, MNRAS, 442, 2304
Hopkins, P. F., Hernquist, L., Cox, T. J., & Kereš, D. 2008, ApJS, 175, 356
Hopkins, P. F., Hernquist, L., Cox, T. J., et al. 2005, ApJ, 630, 705
Hopkins, P. F., Hernquist, L., Cox, T. J., et al. 2006, ApJS, 163, 1
Ilbert, O., McCracken, H. J., Le Fèvre, O., et al. 2013, A&A, 556, A55
Ilbert, O., Salvato, M., Le Floc'h, E., et al. 2010, ApJ, 709, 644
Ishibashi, W., & Fabian, A. C. 2016, MNRAS, 463, 1291
Janz, J., Penny, S. J., Graham, A. W., Forbes, D. A., & Davies, R. L. 2017,
          S. 468, 2850
Joshi, G. D., Pillepich, A., Nelson, D., et al. 2021, MNRAS, 508, 1652
Kauffmann, G., Heckman, T. M., Tremonti, C., et al. 2003a, MNRAS, 346, 1055
Kauffmann, G., Heckman, T. M., White, S. D. M., et al. 2003b, MNRAS,
   341, 54
Kauffmann, G., White, S. D. M., & Guiderdoni, B. 1993, MNRAS, 264, 201
Kauffmann, G., White, S. D. M., Heckman, T. M., et al. 2004, MNRAS,
Kazantzidis, S., Mayer, L., Colpi, M., et al. 2005, ApJL, 623, L67
```

```
Kimm, T., Cen, R., Devriendt, J., Dubois, Y., & Slyz, A. 2015, MNRAS,
   451, 2900
Kimm, T., Somerville, R. S., Yi, S. K., et al. 2009, MNRAS, 394, 1131
Knollmann, S. R., & Knebe, A. 2009, ApJS, 182, 608
Koudmani, S., Henden, N. A., & Sijacki, D. 2021, MNRAS, 503, 3568
Koudmani, S., Sijacki, D., Bourne, M. A., & Smith, M. C. 2019, MNRAS,
   484, 2047
Koudmani, S., Sijacki, D., & Smith, M. C. 2022, MNRAS, 516, 2112
Kroupa, P. 2001, MNRAS, 322, 231
Larson, R. B. 1974, MNRAS, 169, 229
López Fernández, R., González Delgado, R. M., Pérez, E., et al. 2018, A&A,
  615, A27
Manzano-King, C. M., Canalizo, G., & Sales, L. V. 2019, ApJ, 884, 54
Mao, Y.-Y., Geha, M., Wechsler, R. H., et al. 2021, ApJ, 907, 85
Marinacci, F., Vogelsberger, M., Pakmor, R., et al. 2018, MNRAS, 480, 5113
Martin, G., Kaviraj, S., Devriendt, J. E. G., Dubois, Y., & Pichon, C. 2018,
   MNRAS, 480, 2266
Martínez-Delgado, D., Läsker, R., Sharina, M., et al. 2016, AJ, 151, 96
McAlpine, S., Bower, R. G., Rosario, D. J., et al. 2018, MNRAS, 481, 3118
McAlpine, S., Harrison, C. M., Rosario, D. J., et al. 2020, MNRAS, 494, 5713
McGee, S. L., Balogh, M. L., Wilman, D. J., et al. 2011, MNRAS, 413, 996
Menon, H., Wesolowski, L., Zheng, G., et al. 2015, ComAC, 2, 1
Monelli, M., Hidalgo, S. L., Stetson, P. B., et al. 2010, ApJ, 720, 1225
Mori, M., Ferrara, A., & Madau, P. 2002, ApJ, 571, 40
Moster, B. P., Naab, T., & White, S. D. M. 2013, MNRAS, 428, 3121
Munshi, F., Brooks, A. M., Applebaum, E., et al. 2021, ApJ, 923, 35
Munshi, F., Brooks, A. M., Christensen, C., et al. 2019, ApJ, 874, 40
Munshi, F., Governato, F., Brooks, A. M., et al. 2013, ApJ, 766, 56
Muzzin, A., Marchesini, D., Stefanon, M., et al. 2013, ApJ, 777, 18
Naiman, J. P., Pillepich, A., Springel, V., et al. 2018, MNRAS, 477, 1206
Nelson, D., Pillepich, A., Springel, V., et al. 2018, MNRAS, 475, 624
Obreschkow, D., & Glazebrook, K. 2014, ApJ, 784, 26
Okamoto, T., Gao, L., & Theuns, T. 2008, MNRAS, 390, 920
Peng, Y., Lilly, S. J., Kovac, K., et al. 2010, ApJ, 721, 193
Peng, Y., Maiolino, R., & Cochrane, R. 2015, Natur, 521, 192
Penny, S. J., Masters, K. L., Smethurst, R., et al. 2018, MNRAS, 476, 979
Penny, S. J., Masters, K. L., Weijmans, A.-M., et al. 2016, MNRAS, 462, 3955
Pfister, H., Lupi, A., Capelo, P. R., et al. 2017, MNRAS, 471, 3646
Pillepich, A., Nelson, D., Hernquist, L., et al. 2018, MNRAS, 475, 648
Piotrowska, J. M., Bluck, A. F. L., Maiolino, R., & Peng, Y. 2022, MNRAS,
Planck Collaboration, Ade, P. A. R., Aghanim, N., et al. 2014, A&A, 571, A16
Pontzen, A., Tremmel, M., Roth, N., et al. 2017, MNRAS, 465, 547
Power, C., Navarro, J. F., Jenkins, A., et al. 2003, MNRAS, 338, 14
Prole, D. J., van der Burg, R. F. J., Hilker, M., & Spitler, L. R. 2020, MNRAS,
   500, 2049
Rasmussen, J., Mulchaey, J. S., Bai, L., et al. 2012, ApJ, 757, 122
Rees, M. J., & Ostriker, J. P. 1977, MNRAS, 179, 541
Reines, A. E., Condon, J. J., Darling, J., & Greene, J. E. 2020, ApJ, 888, 36
Rey, M. P., Pontzen, A., Agertz, O., et al. 2019, ApJL, 886, L3
Rey, M. P., Pontzen, A., Agertz, O., et al. 2020, MNRAS, 497, 1508
Ricarte, A., Tremmel, M., Natarajan, P., & Quinn, T. 2019, MNRAS, 489, 802
Ricarte, A., Tremmel, M., Natarajan, P., & Quinn, T. 2021a, ApJL, 916, L18
Ricarte, A., Tremmel, M., Natarajan, P., Zimmer, C., & Quinn, T. 2021b,
   MNRAS, 503, 6098
Román, J., Beasley, M. A., Ruiz-Lara, T., & Valls-Gabaud, D. 2019, MNRAS,
```

```
Samuel, J., Wetzel, A., Santistevan, I., et al. 2022, MNRAS, 514, 5276
Sanchez, N. N., Tremmel, M., Werk, J. K., et al. 2021, ApJ, 911, 116
Sanchez, N. N., Werk, J. K., Tremmel, M., et al. 2019, ApJ, 882, 8
Schaye, J., Crain, R. A., Bower, R. G., et al. 2015, MNRAS, 446, 521
Schramm, M., & Silverman, J. D. 2013, ApJ, 767, 13
Sharma, R. S., Brooks, A. M., Somerville, R. S., et al. 2020, ApJ, 897, 103
Sharma, R. S., Brooks, A. M., Tremmel, M., et al. 2022, ApJ, 936, 14
Shen, S., Wadsley, J., & Stinson, G. 2010, MNRAS, 407, 1581
Sijacki, D., Springel, V., Di Matteo, T., & Hernquist, L. 2007, MNRAS,
  380, 877
Silk, J. 2017, ApJL, 839, L13
Simpson, C. M., Grand, R. J. J., Gómez, F. A., et al. 2018, MNRAS,
Skillman, E. D., Monelli, M., Weisz, D. R., et al. 2017, ApJ, 837, 102
Smith, R. J., Lucey, J. R., Price, J., Hudson, M. J., & Phillipps, S. 2012,
  MNRAS, 419, 3167
Snyder, G. F., Torrey, P., Lotz, J. M., et al. 2015, MNRAS, 454, 1886
Somerville, R. S., & Davé, R. 2015, ARA&A, 53, 51
Springel, V., Pakmor, R., Pillepich, A., et al. 2018, MNRAS, 475, 676
Steinborn, L. K., Hirschmann, M., Dolag, K., et al. 2018, MNRAS, 481, 341
Stinson, G., Seth, A., Katz, N., et al. 2006, MNRAS, 373, 1074
Strateva, I., Ivezić, Ž, Knapp, G. R., et al. 2001, AJ, 122, 1861
Thanjavur, K., Simard, L., Bluck, A. F. L., & Mendel, T. 2016, MNRAS,
  459, 44
Tinker, J., Wetzel, A., & Conroy, C. 2011, arXiv:1107.5046
Tinker, J. L., Wetzel, A. R., Conroy, C., & Mao, Y.-Y. 2017, MNRAS,
  472, 2504
Tonnesen, S., Bryan, G. L., & van Gorkom, J. H. 2007, ApJ, 671, 1434
Tremmel, M., Governato, F., Volonteri, M., Pontzen, A., & Quinn, T. R. 2018,
  ApJL, 857, L22
Tremmel, M., Governato, F., Volonteri, M., & Quinn, T. R. 2015, MNRAS,
  451, 1868
Tremmel, M., Karcher, M., Governato, F., et al. 2017, MNRAS, 470, 1121
Tremmel, M., Quinn, T. R., Ricarte, A., et al. 2019, MNRAS, 483, 3336
Trussler, J., Maiolino, R., Maraston, C., et al. 2020, MNRAS, 491, 5406
van den Bosch, F. C., Aquino, D., Yang, X., et al. 2008, MNRAS, 387, 79
Villaume, A., Conroy, C., & Johnson, B. D. 2015, ApJ, 806, 82
Volonteri, M. 2012, Sci, 337, 544
Volonteri, M., & Natarajan, P. 2009, MNRAS, 400, 1911
Wadsley, J. W., Keller, B. W., & Quinn, T. R. 2017, MNRAS, 471, 2357
Weinberger, R., Springel, V., Hernquist, L., et al. 2017, MNRAS, 465, 3291
Weinmann, S. M., Kauffmann, G., van den Bosch, F. C., et al. 2009, MNRAS,
  394, 1213
Weinmann, S. M., van den Bosch, F. C., Yang, X., & Mo, H. J. 2006,
  MNRAS, 366, 2
Weisz, D. R., Dolphin, A. E., Skillman, E. D., et al. 2014, ApJ, 789, 148
Weisz, D. R., Dolphin, A. E., Skillman, E. D., et al. 2015, ApJ, 804, 136
Wetzel, A. R., Tinker, J. L., & Conroy, C. 2012, MNRAS, 424, 232
Wetzel, A. R., Tinker, J. L., Conroy, C., & van den Bosch, F. C. 2013,
   MNRAS, 432, 336
Wetzel, A. R., Tinker, J. L., Conroy, C., & van den Bosch, F. C. 2014,
   MNRAS, 439, 2687
Wild, V., Almaini, O., Dunlop, J., et al. 2016, MNRAS, 463, 832
Wild, V., Walcher, C. J., Johansson, P. H., et al. 2009, MNRAS, 395, 144
Willmer, C. N. A., Faber, S. M., Koo, D. C., et al. 2006, ApJ, 647, 853
Wyder, T. K., Martin, D. C., Schiminovich, D., et al. 2007, ApJS, 173, 293
```

Yan, R., Newman, J. A., Faber, S. M., et al. 2006, ApJ, 648, 281